Review

TiO$_2$–SrTiO$_3$ Biphase Nanoceramics as Advanced Thermoelectric Materials

Alexey Zavjalov *, Sergey Tikhonov * and **Denis Kosyanov ***

School of Natural Sciences, Far Eastern Federal University, 8 Sukhanova Street,
Vladivostok 690950, Russian Federation

* Correspondence: Zav_Alexey@list.ru (A.Z.); Allser@bk.ru (S.T.); Kosianov.diu@dvfu.ru (D.K.);
Tel.: +7-999-616-2084 (A.Z.); +7-914-338-2974 (S.T.); +7-984-156-6480 (D.K.)

check for updates

Abstract: The review embraces a number of research papers concerning the fabrication of oxide thermoelectric systems, with TiO$_2$–SrTiO$_3$ biphase ceramics being emphasized. The ceramics is particularly known for a two-dimensional electron gas (2DEG) forming spontaneously on the TiO$_2$/SrTiO$_3$ heterointerface (modulation doping), unlike ordinary 2DEG occurrence on specially fabricated thin film. Such effect is provided by the SrTiO$_3$ conduction band edge being 0.40 and 0.20 eV higher than that for anatase and rutile TiO$_2$, respectively. That is why, in the case of a checkered arrangement of TiO$_2$ and SrTiO$_3$ grains, the united 2D net is probably formed along the grain boundaries with 2DEG occurring there. To reach such conditions, there should be applied novelties in the field of ceramics materials science, because it is important to obtain highly dense material preserving small (nanoscale) grain size and thin interface boundary. The review also discusses some aspects of reactive spark plasma sintering as a promising method of preparing perovskite-oxide TiO$_2$–SrTiO$_3$ thermoelectric materials for high-temperature applications.

Keywords: SrTiO$_3$; TiO$_2$; biphase nanoceramics; two-dimensional electron gas; 2DEG; thermoelectric efficiency; thermoelectric efficiency *ZT*; spark plasma sintering; SPS; oxide thermoelectric materials

1. Introduction

Today, a large part of energy is produced by heat machines leading to a high amount of heat being dissipated (60% of total energy) into the environment due to known physical limitations [1]. Therefore, secondary exhaust heat processing is highly promising for energy efficiency improvement. One of the ways to do that is the direct consumption of exhaust heat, which is the valuable resource itself, right in the power plants. However, this method is rather limited [2] in its ability to satisfy growing energy consumption and to reduce the usage of conventional fuels, thus, new alternative and effective ways to convert the excess heat into energy are in high demand.

Special attention in this respect is given to technologies of direct heat conversion into electric power [3–6]. Experimental and theoretical investigations in order to understand the mechanisms involved and to improve the materials properties and conversion efficiency have been ongoing for more than half a century. Particularly, Figure 1 shows the statistics of review papers from 1995 to 2018 on "Thermoelectric", "Thermoelectric oxide" and "Thermoelectric oxide nano" queries. The annual amount of research has increased more than 20-fold (from 12 in 1995 to 260 in 2018). The highest publication activity in this field is happening now: From 2014, the number of published reviews grew by 40 every year, which corresponds to additional 1000 research papers. They are focused mainly on the thermoelectric properties of oxides and thermoelectric devices based on them (over 50% of papers have studied oxide systems since 2014) (Figure 1).
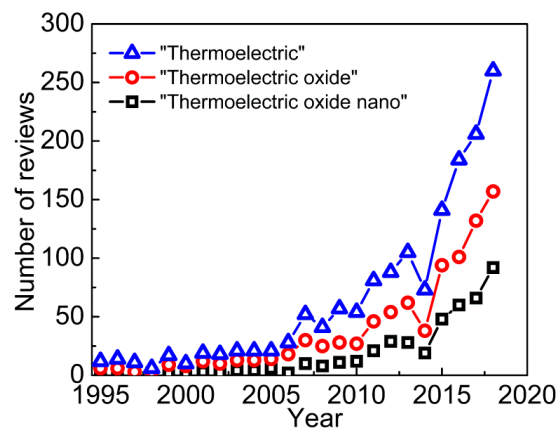
Figure 1. Statistics on review papers from 1995 to 2018 on ScienceDirect on queries "Thermoelectric", "Thermoelectric oxide" and "Thermoelectric oxide nano".

Historically, thermoelectric energy conversion started in 1821, when T.J. Seebeck described the occurrence of voltage on the ends of conductor that are exposed to different temperatures [7]. To some extent, the reverse effect of occurring temperature difference was observed by J.C.A. Peltier for the heterometallic circuit under voltage [8]. Both effects are named after their discoverers and serve as a basis for modern devices of secondary processing of exhaust heat and for heat pumps.

The coefficient of power efficiency for the thermoelectric converter η is evaluated as follows Equation (1) [9–11]:

$$\eta = \frac{T_h - T_c}{T_h} \frac{M - 1}{M + (T_c/T_h)}, \tag{1}$$

$$M = \sqrt{1 + Z(T_h + T_c)/2}, \tag{2}$$

where T_h and T_c—temperature of hot and cold side, respectively; Z—thermoelectric quality factor.

At the same time, the key thermoelectric feature is the thermoelectric efficiency ZT, which is a dimensionless value [12]. The most widely used thermoelectrics at the moment, Bi_2Te_3 and PbTe, are characterized by $ZT\sim1$ that determines the borderline of the application of these materials on a large scale [13,14]. Additionally, alloys based on heavy metals with $ZT > 1$ are obtained, thus, expanding the horizons of thermoelectric generators applications [14–23]. However, many technological processes produce exhaust heat at high temperatures (the temperature of an exhaust pipe is ~700 °C). Under such conditions, partial thermal decomposition of the mentioned materials takes place leading to contamination of the environment with wastes containing heavy and/or toxic metals. Radioisotope thermoelectric generators (RITEGs) are a good example of the solution to this problem, where heat of radioactive decomposition is converted into electric energy. The striking example of using RITEG is space probe "Voyager-2", the most distant evidence of human beings out of Earth. There is SiGe-based semiconductor thermoelectric material installed on "Voyager-2", which produces electricity from the heat of the plutonium core at 1000 °C with the ZT value reaching 1 only at such elevated temperatures [24]. Similar systems of autonomous power supply are used in many other ground-level frames (radio beacon, weather stations and etc.). It is noteworthy that indicated temperatures are extreme for silicide materials [5], i.e., there is a need for thermoelectric materials that are stable at such temperatures (and radiation background).

Above 1000 °C, oxide compounds are well thermally and chemically stable. They can be applied either as separate materials [10,11,25] or as a high-temperature layer in the composite thermoelectric systems [11]. J.R. Szczech et al. have shown that thermoelectric efficiency can be drastically enhanced if nanostructured materials are used [26]. The last decade's achievements and prospects are fully reported in Chapters 22, 23 of the review "Nanotechnology for Energy Sustainability" [5]. Special attention should be paid to the work by H. Ohta et al., which presents a pulse laser sputtering

method for $SrTiO_3/TiO_2$ bi-layered system fabrication [27]. The main feature of that composite is that two-dimensional electron gas (2DEG) occurs not in the specially formed thin layer as usual, but in the interface region of $SrTiO_3/TiO_2$ ceramics. Therefore, if grains of $SrTiO_3$ and TiO_2 are checkered, then the unified coherent 2D surface is obtained along the grain boundaries providing 2DEG formation. But there is no research addressing this issue. A similar structure is proposed by K. Koumoto et al. only as a hypothesis [10]. The authors recommend a preparation of $SrTiO_3$ material with 10 at.% of La ions in Sr positions being separated by thin layers of 20 at.% of Nb ions in Ti positions. Alternatively, similar material should be obtained as a ceramic that utilizes 2DEG features in thin layers. In that case, ceramic novelties should be applied to achieve minimal thickness of the separation layer. Anyway, the adaptation of methods of large-scale production for ceramics can provide available and highly efficient thermoelectric materials for a broad range of practical applications. In view of the above, the review is devoted to the search of a new approach to fabricate thermoelectric oxide materials based on bi-phase $SrTiO_3$-based ceramics. This review will ultimately attempt to answer the question, "Is it possible to further improve the thermoelectric properties of $SrTiO_3$-based ceramics?"

2. Oxide Thermoelectrics History

H. Ohta distinguished the three main periods of oxide thermoelectric research [1]. The first papers published in the 1950s–1970s studied thermoelectric characteristics of simple oxides, such as CdO [28], NiO [29], ZnO [30], In_2O_3 [31], $SrTiO_3$ [32], rutile-TiO_2 [33], SnO_2 [34], and Cu_2O [35]. In 1986, two IBM employees, K. Muller and G. Bednorz, discovered high-temperature superconductivity for the $La_{2-x}Ba_xCuO_4$ system [36] and consequently won the Nobel Prize in physics in 1987. However, the real breakthrough in a plethora of fields occurred after the discovery of superconductivity in the $YBa_2Cu_3O_{7-x}$ system (77 K) in 1987, because fairly cheap liquid nitrogen enabled researchers to achieve a superconductive state in that case [37]. Then, the second stage of studying thermoelectric properties of high-temperature superconductive oxides began: La_2CuO_4 [38], La–Ba–Cu–O [39], $YBa_2Cu_3O_{7-\delta}$ [40], Tl–Ca–Ba–Cu–O [41] and etc. The third stage in thermoelectric oxide research demonstrated high *ZT* values for simpler oxide systems as $CaMnO_3$ [42], Al-doped ZnO [43], Na_xCoO_2 [44], $Ca_3Co_4O_9$ ($Ca_2Co_2O_5$) [45,46] and electron-doped $SrTiO_3$ [47–50]. Data on these systems presented up to 2012 show their *ZT* values were still below 1 [50]: $Ca_3Co_4O_9$ (0.15–0.5 at 1000 K), Na_xCoO_2 (0.3–0.9 at 950 K), $SrTiO_3$ (0.2–0.35 at 1000 K), $CaMnO_3$ (0.1–0.2 at 1000 K), and ZnO (0.03–0.5 at 1073 K).

The general trend in research has been shifting towards low-sized (including nano-) thermoelectric systems for more than 20 years already (Figure 1). Apparently, that has happened because the "classical" methods of improving oxide's thermoelectric characteristics (e.g., doping with rare earth metals and/or creating point defects) have become nearly exhausted. At the same time, new effects have been observed on a nanoscale, namely, two-dimensional electron gas (2DEG) can be formed in the material. In other words, we are observing the fourth stage of oxide thermoelectric research at the moment.

3. Theoretical Aspects of Thermoelectricity

As it was mentioned above Equations (1) and (2), thermoelectric efficiency of the material is often assessed in terms of figure of merit *ZT* (Equation (3)) [12]:

$$ZT = S^2\sigma T/\kappa, \tag{3}$$

where S is Seebeck's coefficient (thermal emf); σ is electrical conductivity; κ is thermal conductivity.

Improving the *ZT* value (Equation (3)) boils down to increasing the power factor ($S^2\sigma$) and reducing thermal conductivity κ. Although theoretical limit for *ZT* is absent [51], thermoelectric parameters in practice are deeply connected with each other and improvement in one worsens the other, thus, having no effect on the *ZT* value.

The main contribution to thermal conductivity comes from phonons and charge carriers, that is why the whole thermal conductivity of the materials is a sum of their partial contributions (Equation (4)) [52]:

$$\kappa = \kappa_{ph} + \kappa_e, \tag{4}$$

Gas kinetic theory for solids determines electron and phonon thermal conductivity according to general principles (Equations (5) and (6)) [52]:

$$\kappa_{ph} = \frac{1}{3} C_v v_s L_{ph}, \tag{5}$$

$$\kappa_e = \frac{1}{3} c_v v \Lambda, \tag{6}$$

where v_s—sound velocity; C_v—thermal capacity at constant volume; L_{ph}—phonon's mean free path (MFP) controlled by phonon-phonon distance [53]; c_v—electrons' specific thermal capacity per unit volume; v—mean electron velocity that can be taken as Fermi velocity v_F; Λ—electron's mean free path.

According to the Wiedemann–Franz relationship [54], electron thermal conductivity (Equation (6)) can be given by:

$$\kappa_e = L\sigma T, \tag{7}$$

where L—Lorentz number 2.45×10^{-8} V^2/K^2.

As it follows from Equation (7), electrical conductivity decreases with electron thermal conductivity. However, acoustic phonons κ_{ph} contributes more to thermal conductivity (Equation (4)) in case of semiconductors and insulators (although its value can be lower as compared to electron conductivity in highly alloyed and non-stoichiometric systems) [52].

Phonon thermal conductivity is the only parameter which is not defined by electron structure and, therefore, does not depend on other parameters [55]. That is why many researchers try to minimize it close to theoretical value (0.25–0.50 Wm^{-1}·K^{-1}) via confining phonon MFP down to interatomic distance [56]. It is noteworthy that idea of improving the *ZT* value via simultaneous increasing electrical conductivity σ and decreasing phonon thermal conductivity κ_{ph} serves as a basis for the "Phonon glass–electron crystal" (PGEC) concept [3]. PGEC materials work as crystals for electrons, providing good conductivity, and dissipate phonons as well, like glasses, thus reducing phonon thermal conductivity. The theoretical *ZT* value of ~4 at 77–300 K for such materials is given in [51]. However, the *ZT* value for such systems does exceed 1 due to the introduction of special sites dissipating phonons (such as skutterudites, clathrates, and zintle phases) into the material's bulk [5].

Obviously, there is no formula connecting the phonon thermal conductivity κ_{ph} with other thermoelectric characteristics in the presented review. In practice, thermoelectric characteristics are often affected by the material's structure, which has a complex effect on all the parameters of the material as a thermoelectric. From this point of view, let us consider several experimental works studying SrTiO$_3$-based materials that are an objective of the present review.

Reference [52] (referring to [10]) indicates that low ZT values for SrTiO$_3$-based materials are caused by their high thermal conductivity κ_{ph}. This work also notes that point defects of alloying agents are not effective phonon dissipation sites [52]. Therefore, changing the power factor ($S^2\sigma$) by introducing ligands can be done without an impact on thermal conductivity κ_{ph}. As an efficient way to reduce thermal conductivity κ, H. Muta et al. suggested to provide structural defects via substitution of Sr^{2+} with Ca^{2+} or Ba^{2+} in titanates solid solutions, because this type of defect will act as phonon dissipation sites [57,58]. However, such substitution may lead to significant asymmetry with thermal conductivity reduction being compensated by lowering the power factor $S^2\sigma$ [59]. At the same time, semiisovalent substitution of Sr^{2+} with Eu^{2+} has practically no effect on power factor $S^2\sigma$ and reduces phonon's MFP by ~12%, but considerable decrease of the overall thermal conductivity is observed only at $T < 400$K [60]. Such type of substitution is unusable because oxide compounds are considered as promising thermoelectric materials for high-temperature applications (>1000 °C).

Special attention should be paid for double alloying of $SrTiO_3$-based thermoelectrics. Diversity of dissipation sites in the crystal lattice always enhances thermal conductivity reduction κ: $(Sr_{1-x-y}La_xYb_y)TiO_3$ [61], $Sr_{1-x}(Ti_{1-y-z}Nb_yW_z)O_{3\pm\delta}$ [62], $(Sr_{1-x}La_x)(Ti_{1-x}Ta_x)O_3$ and $(Sr_{1-x}La_x)(Ti_{1-x}Nb_x)O_3$ [63]. On the other hand, conductivity and Seebeck's coefficient are also affected in a way depending on the quantity and/or the type of point defects. More in-depth information on alloying effects on thermoelectric properties can be found in some review papers [11,52,64].

Additionally, phonon dissipation to suppress κ_{ph} is not an ultimate goal. Modelling has shown [65] that there are spectrally different groups of phonons responsible for heat transfer and electron drag towards the temperature gradient. The latter phonons contribute more or less significantly to thermo-emf (Seebeck effect) S at least at low temperatures. The phonon drag contribution to thermo-emf S is often observed for electron-doped systems [27,32,47,66]. Therefore, when developing thermoelectric materials, it is important to prepare filters suppressing heat transferring phonons and transmitting electron dragging ones that can enhance the ZT value of the material (at least for low temperatures) [65].

Power factor ($S^2\sigma$) consists of two components. Conductivity can be written as Equation (8) [67]:

$$\sigma = \int_0^{+\infty} \sigma(E)\left(-\frac{\partial f(E)}{\partial E}\right)dE, \tag{8}$$

where $\sigma(E)$—differential conductivity (the electrical conductivity of the electrons that fill the energy levels between E and $E + dE$), $f(E)$—the Fermi distribution function.

Then, thermo-emf S is determined by Mott's Equation (9):

$$S = \frac{1}{e\sigma T}\int_0^{+\infty} \sigma(E)(E - E_F)\left(\frac{\partial f(E)}{\partial E}\right)dE, \tag{9}$$

where E_F—Fermi energy, e—elementary charge.

Thus, both components of power factor, Equations (8) and (9), are governed by differential conductivity $\sigma(E)$ and by differential mobility $\mu(E)$: $\sigma(E)$ is evaluated through density of charge carriers $n(E)$ via density of states calculation (DOS) $g(E)$; $\mu(E)$ depends on relaxation time $\tau(E)$ and effective mass m^* (Equations (10–12)):

$$\sigma(E) = n(E)e\mu(E), \tag{10}$$

$$n(E) = g(E)f(E), \tag{11}$$

$$\mu(E) = e\frac{\tau(E)}{m^*}, \tag{12}$$

The power factor is given by the following expression (Equation (13)):

$$S^2\sigma = \frac{1}{e^2T^2}\frac{\left(\int_0^{+\infty} n(E)e\mu(E)(E - E_F)\left(\frac{\partial f(E)}{\partial E}\right)dE\right)^2}{\int_0^{+\infty} n(E)e\mu(E)\left(-\frac{\partial f(E)}{\partial E}\right)dE}, \tag{13}$$

As it comes from Equation (13), the higher charge carriers' concentration the higher power factor that is applied in n-type semiconductors (e.g., via alloying till their degeneration). In metals and degenerate semiconductors, Fermi statistics can be considered degenerate and expression for conductivity (Equation (8)) is simplified to a "metal" one and Mott's equation (Equation (9)) becomes more ordinary "metal-like" (Equations (14) and (15)) [67]:

$$\sigma = \sigma(E_F) = n(E_F)e\mu(E_F), \tag{14}$$

$$S = \frac{\pi^2 k_B^2}{3e}T\left\{\frac{dln\sigma(E)}{dE}\right\}_{E=E_F} = \frac{\pi^2 k_B^2}{3e}T\left\{\frac{1}{n}\frac{dn(E)}{dE} + \frac{1}{\mu}\frac{d\mu(E)}{dE}\right\}_{E=E_F}, \tag{15}$$

Although Equations (14) and (15) correspond to the limit case, they fit well to demonstrate the influence of such factors as charge carrier concentration $n(E)$ and differential mobility $\mu(E)$ on thermoelectric properties of the material. As it follows from Equation (14), higher concentration n and mobility μ of charge carriers increases their conductivity σ, while the Seebeck's effect (Equation (15)) is governed by their differential characteristics. Let us consider two routes to change thermo-emf in more detail [68].

The first term in Equation (15) is $dn(E)/dE$, which is determined by DOS function behavior (Equation (11)). Figure 2 shows the general behavior of the DOS function [68].
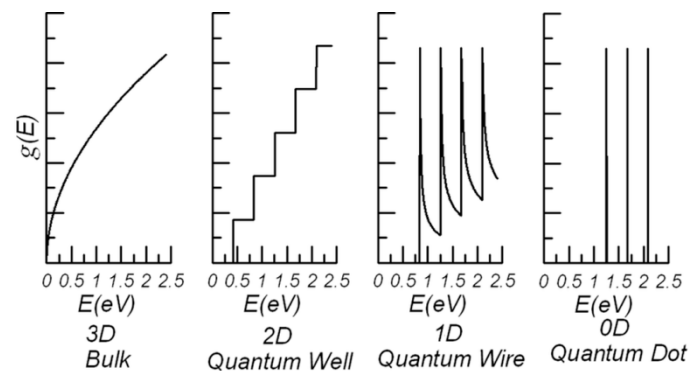

Figure 2. General behavior of the DOS function in the systems of different dimensionality. Reproduced with permission from Ref. [68]. Copyright 2005, *Acta Physica Polonica A*: Institute of Physics, Polish Academy of Sciences.

Contrary to 3D systems, $dn(E)/dE$ may take high values in the systems with less degrees of freedom due to the size-quantization effect on $g(E)$. That is why nanostructured materials may exhibit higher ZT values, because electron gas can be confined there. Obviously, the phonon thermal conductivity becomes reduced in low-dimension systems due to intensive dissipation on the boundaries. Concerning practical applications, low-dimension systems should be prepared via nanoengineering methods in the volume of 3D thermoelectric material. Therefore, the same boundaries play a positive role as phonon dissipation sites to reduce thermal conductivity and size of the bulk thermoelectric or even may act as phonon filters according to the concept presented above.

The second term in Equation (15) is $d\mu(E)/dE$, which is determined by behavior or time relaxation function $\tau(E)$ (Equation (12)). In other words, to increase thermo-emf one needs to achieve strong dependence of electrons dissipation on their energy, i.e., filtration of electron with respect to energy. The paper [68] referred to several examples of such filtration with different efficiency, however, the present review addresses the latest theoretical work [69]. It treats 2DEG as an energy barrier for electrons from the bulk on the grain boundaries. When calculating the thermoelectric characteristics of the material, the lower limit in the energy integrals in Equations (14) and (15) corresponds to this energy barrier. Such approach is quite inaccurate, because it is based on classical physics and does consider electron tunneling through the barrier. Anyway, it demonstrates qualitatively that filtration of bulk electrons amplifies ZT by a factor of 1.5 at optimal barrier height, which slightly exceeds the Fermi level. This agrees well with the point stating the significance of $\tau(E)$ dependence in the region of Fermi level according to the metal-like Equation (15) for S.

To summarize the theoretical aspects of thermoelectricity, nanostructured materials should possess enhanced thermoelectric characteristics. The diversified net of mutually connected boundaries in the bulk nano-thermoelectric can serve as phonon filters (important for low temperatures) or simply as sites for phonon dissipation. The 2DEG state appearing there can act as electron filters to improve thermoelectric characteristics of the bulk materials as well as form an individual low-dimension phase with enhanced thermoelectric properties improving the overall material's characteristics.

4. Thermoelectricity on Oxides Interfaces

4.1. Oxide Heterointerfaces

As shown in Section 3, multiple boundaries in the bulk thermoelectric can play a positive role in increasing phonon dissipation and decreasing thermal conductivity, as demonstrated by K. Koumoto et al. for $SrTiO_3$ [10] (Figure 3). Additionally, there may be formed regions of 2DEG localization on the grain boundaries of the oxide materials.
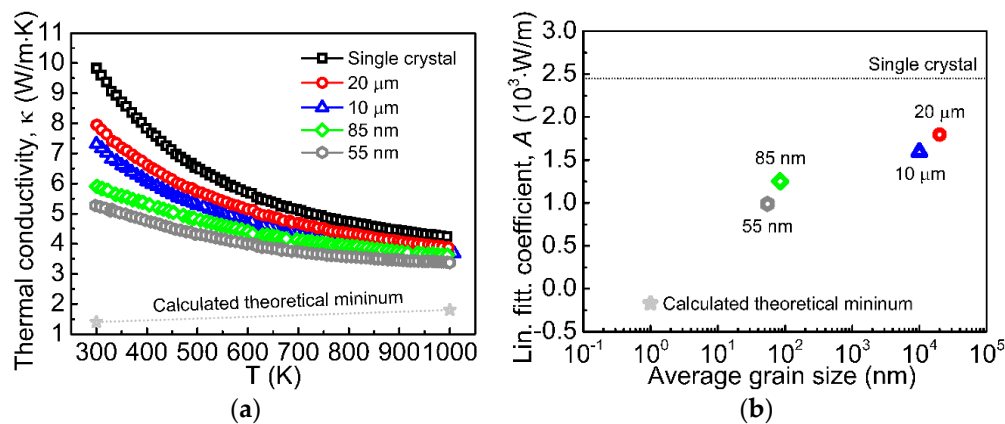

Figure 3. Temperature dependence (**a**) of effective thermal conductivity for $SrTiO_3$ polycrystalline ceramics and single crystal (also shows a calculated theoretical minimum for disordered crystals with few nm grain size). Size dependence (**b**) of linear coefficient A for fitting $\kappa(T) = \kappa_o + A/T + B/T^2$. Estimated average grain sizes are shown for some representative samples according to Reference [10].

A striking example is the $LaAlO_3/SrTiO_3$ system, for which A. Ohtomo et al. showed 2DEG formation with high electron mobility [70]. It arises due to polarity discontinuity between alternating polar lattice $(AlO_2)^-/(LaO)^+$ and neutral one $(TiO_2)^0/(SrO)^0$. Electron mobility in the interface $(LaO)^+/(TiO_2)^o$ appeared rather high for observing dramatic periodic oscillations of magnetoresistance at low temperatures (2–5 K) in response to magnetic field inversion, which indicates quantum transport. N. Reyren et al. demonstrated 2D superconductivity for that 2DEG with $T_s = 0.2$ K in 2007 [71]. And finally, in 2016, I. Pallecchi et al. revealed a large contribution of phonon drag to thermo-emf when studying the thermoelectric properties of the $LaAlO_3/SrTiO_3$ boundary at low temperatures (<50 K, peak at ~12–14 K) [72]. Formation of 2DEG via the similar mechanism on the hetero interface $(LaO)^+/(TiO_2)^0$ was shown for the $LaGaO_3/SrTiO_3$ system [73].

The mechanism is a rather universal one for complex perovskite-type oxides with the general formula ABO_3 (where A—alkali-earth or rare-earth metal, B—transition 3d, 4d or 5d metal) [74]. As an example, let us consider $RTiO_3/SrTiO_3$-type hetero interfaces (where R—rare earth metal) [75–79]. There are alternating atomic layers $RO/TiO_2/SrO$ on the boundary. Titanium ions in the middle layer (TiO_2) exhibit a "struggle" between oxidation states +3 and +4. In the sequence of $(Ti^{4+}O_2{}^{4-})^0/(Sr^{2+}O^{4-})^0$ layers of $SrTiO_3$ structure, TiO_2 layer should be neutral, while in the sequence of $(R^{3+}O^{2-})^{+1}/(Ti^{3+}O_2{}^{4-})^{-1}$ layers it should be charged. As a result, $(R^{3+}O^{2-})^{+1}$ layer acts as donor of electrons for the TiO_2 layer leading to the 2DEG formation on it. From another point of view, when R acts as alloying agent for $SrTiO_3$, but alloying occurs only along phase boundary. Beyond that, as in ordinary alloying, R acts as an electron donor. Another feature of such "planar" alloying is the absence of alloying agent in the region of 2DEG localization, which leads to absence of dissipation of electrons on R+ ions in the crystal lattice (this effect cannot be achieved for 3DEG at bulk material alloying). It is noteworthy that additional alloying of $SrTiO_3$ bulk phase with reasonable amount of electron donors does not lead to its spontaneous polarization, while additional electrons attracted by arbitrarily positive $(RO)^{+1}$ layer on the grain boundary should increase the density of 2DEG [77].

Obviously, in more general case the contact between polar and nonpolar materials is not obligatory, but the main point is the unbalanced polarizations between the layers on the boundary. For example, $Mg_xZn_{1-x}O/ZnO$ hetero structure consisting of piezoelectric materials exhibit 2DEG formation on the boundary, because the piezo-effect (caused by stress due to different lattice parameters) leads to unbalanced polarization and 2DEG formation [80–83]. This allowed the observation, for the first time, of the quantum Hall effect in the oxide system based on $Mg_{0.15}Zn_{0.85}O/ZnO$ [80] in 2007, and in 2010, A. Tsukazaki et al. demonstrated a fractional quantum Hall effect [81].

Another mechanism of 2DEG formation on the hetero interface of oxide materials is modulation doping [74]. Electrons from the n-doped material tend to leave it and to occupy the second material at the contact, because the conduction band edge of the first material is higher than in the second one (Figure 4). At the same time, there occurs a non-compensated bulk charge in the first material that distorts the conduction bands locally in the region of the contact with the second material. This yield in electron trap occurring in undoped material near the interface boundary and it is thin enough to form 2DEG. The undoped layer of the material with higher conduction band edge enhances this effect (Figure 4) [74].
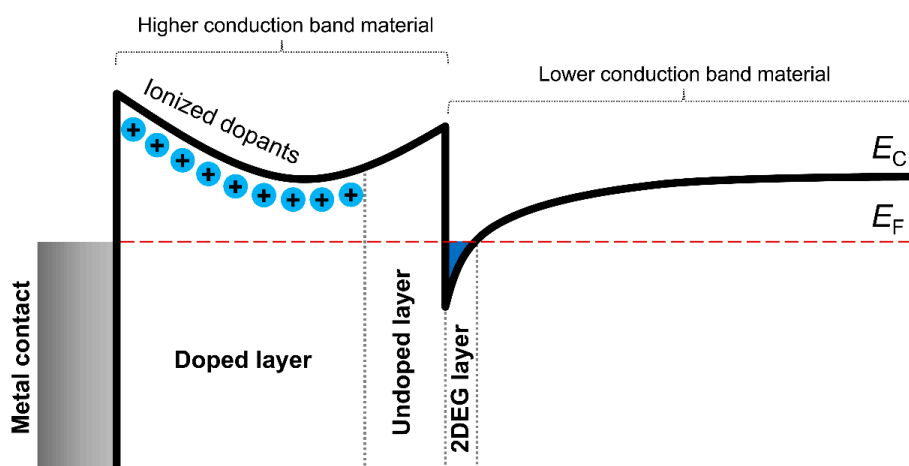

Figure 4. Principle of modulation doping to obtain a high-mobility 2DEG according Ref. [74].

Modulation doping is fairly known and used in heterostructures of AlGaAs/GaAs [84–88]. But that approach is suitable for oxide hetero interfaces. For example, S. Stemmer and S. James Allen suggested considering perovskite hetero interfaces $SrTiO_3/LaAlO_3$ and $SrTiO_3/SrZrO_3$, because the conduction band edge of $SrTiO_3$ [89–92] is lower than that for $LaAlO_3$ and $SrZrO_3$ [93–95]. Formation of 2DEG on the hetero interface of $SrTiO_3$ and n-doped $SrZrO_3$ perovskites are proved by the results of numerical modeling [96] and by modulation doping experiments for $SrTiO_3/Sr(Ti,Zr)O_3$ [97]. 2DEG formation was also demonstrated for the hetero interface of structurally different oxides, $TiO_2/SrTiO_3$ [27].

Recently, Jun-ichi Fujisawa et al. evaluated conduction-band edges for these oxides and showed that the conduction-band edge of $SrTiO_3$ is 0.40 eV higher than for TiO_2 (i.e., modulation doping of $TiO_2/SrTiO_3$ hetero interface is plausible) [98]. It is noteworthy that there were studies on undoped TiO_2 grown on $SrTiO_3$ [27]. The authors claimed that TiO_2 epitaxial films formed by pulsed laser deposition (PLD) may lack oxygen, which is extracted from $SrTiO_3$ yielding the $TiO_2/SrTiO_{3-\delta}$ hetero interface. It is known for $SrTiO_3$ that oxygen-deficiency is equivalent in some way to substituting Sr with La [99]. Therefore, it can be concluded that 2DEG formation on the $TiO_2/SrTiO_3$ hetero interface described in [27] is caused by modulation doping.

4.2. Thermoelectric Properties of Superlattices and Heterointerfaces Based on $SrTiO_3$ Oxide

Let us consider several important works regarding the theme of our review followed by the idea explanation. First of all, let us pay attention to [100], which studies thermoelectric properties

of superlattices based on $SrTiO_{3-\delta}$, fabricated using PLD. The superlattices consisted of pairs of layers with 5 at.% of Sr being substituted with Pr ($(Sr_{0.95}Pr_{0.05})TiO_3$) and 20 at.% Ti ions being substituted with Nb ($Sr(Ti_{0.8}Nb_{0.2})O_3$). The whole series of the studied systems can be presented as $[(Sr_{0.95}Pr_{0.05})TiO_{3-\delta}]_x/[Sr(Ti_{0.8}Nb_{0.2})O_{3-\delta}]_y$ for pairs of (x, y) ∈ {(x, 0); (8, 2); (8, 5); (8, 8); (5, 8); (2, 8); (0, y)}. Superlattices were composed of 20 pairs of layers (x,y) with the layer thickness for determination of their individual characteristics ((x, 0) and (0, y)) being ~500 nm (at least for thermal conductivity measurements).

Temperature dependence on planar conductivity σ [100] and Seebeck's coefficient *S* for superlattices are not somewhat extraordinary (obviously, also the power factor $S^2\sigma$) and change gradually from individual characteristics of two types (from $(Sr_{0.95}Pr_{0.05})TiO_3$ to $Sr(Ti_{0.8}Nb_{0.2})O_3$ and vice versa). Thus, dependences can be described by the model of parallel arranging of independent layers. That means formation of 2DEG was not observed in the studied systems, which will be explained later in the review.

Unfortunately, paper [100] did not include direct temperature dependences of planar thermal conductivity κ. Only $\kappa(T)$ was found in the transverse direction separately for $(Sr_{0.95}Pr_{0.05})TiO_3$ and $Sr(Ti_{0.8}Nb_{0.2})O_3$ layers of large thickness ~500 nm. Comparison was done for layers' thickness ranging from ~0.8 nm for 2 unit cell to ~3.1 nm for 8 unit cell, which is assumed to be equal in thermal conductivity in planar direction due to the isotropic character of the materials properties with cubic crystal structure. For superlattices, temperature dependence κ in planar direction was assessed within the model of parallel thermoresistance. The authors in [100] admit that real thermal conductivity have to be lower mainly due to additional dissipation on hetero interfaces.

Based on obtained κ assessment and measured values of σ and *S*, the work [100] also provides an evaluation of the *ZT* value. It was unexpectedly found that maximal temperature characteristic with respect to the *ZT* value was shown by superlattice (8, 8) with 0.11 value at 300 K and 0.46 at 1000 K. Because thermal conductivity value was overestimated, the *ZT* value is underestimated. The final conclusion on true values can be done via direct measurements of $\kappa(T)$ in planar direction for such superlattices. Anyway, it is revealing that bicomponent system without specific 2D effects can be improved regarding the *ZT* value via optimal adjustment of components ratio with the optimum being at 1:1 ratio.

There is a series of works that studied the influence of component ratio in the superlattice on its thermoelectric characteristics [27,101,102]. $[SrTiO_3]_x/[Sr(Ti_{0.8}Nb_{0.2})O_3]_y$ systems were studied with x = 1–60 and y = 1–20 for 20, 24, and 100 pairs of layers fabricated also using the PLD method. Thermo-emf (Seebeck's coefficient) *S* in the planar direction was chosen as a key thermoelectric characteristic for these superlattices. *S* value was shown to be 320 μV/K at 300 K (5 times higher than 61 μV/K achieved for bulk $Sr(Ti_{0.8}Nb_{0.2})O_3$) for 1 unit cell layers of degenerate insulator $Sr(Ti_{0.8}Nb_{0.2})O_3$ isolated by rather thick (>16 unit cells) layers of nondegenerate $SrTiO_3$ insulator. The thermo-emf of $Sr(Ti_{0.8}Nb_{0.2})O_3$ conducting layer is inversely proportional to the square of its thickness (Figure 5a), as it should be for 2DEG [52]. When thickness reaches 16 unit cell, *S* value is nearly the same as for the bulk material that can be interpreted as 2DEG failure. 2DEG was also shown to be affected by the thickness of $SrTiO_3$ insulating layer (Figure 5b). The *S* value of the conducting $Sr(Ti_{0.8}Nb_{0.2})O_3$ of variable thickness is observed to decrease when the thickness of insulating $SrTiO_3$ is below 6.25 nm (16 unit cells) reaching the value or the bulk $Sr(Ti_{0.8}Nb_{0.2})O_3$ at 0 unit cell of $SrTiO_3$.

In the first case, electron gas localization and 2DEG formation is caused directly by the thickness of the conducting layer, i.e., confinement of the electrons space. In the second case the situation is a bit more complicated. Strict localization of the electron gas in the $Sr(Ti_{0.8}Nb_{0.2})O_3$ layer fails due to electron tunneling through the $SrTiO_3$ insulating layer, namely, the thinner $SrTiO_3$ the less localized electrons become in the $Sr(Ti_{0.8}Nb_{0.2})O_3$ layer leading to gradual failure of 2DEG state.

Taking into account the results of [27,101,102] it is clear why authors in [100] did not observe 2DEG formation. Both systems are similar in some way, because in both cases good conducting $Sr(Ti_{0.8}Nb_{0.2})O_3$ layers alternate with insulating ones. Thus, in [100], conductivity of $(Sr_{0.95}Pr_{0.05})TiO_3$

was only 18 S/cm at 300 K as compared to 3504 S/cm for $Sr(Ti_{0.8}Nb_{0.2})O_3$, while the best candidate for 2DEG among the considered superlattices is the $[(Sr_{0.95}Pr_{0.05})TiO_{3-\delta}]_8/[Sr(Ti_{0.8}Nb_{0.2})O_{3-\delta}]_2$ system. According to [27,101,102], 2 unit cells thickness of the conducting layer drastically weakens 2DEG, the same does 8 unit cells of insulating layer causing delocalization of electron gas due to tunneling. Additionally, $(Sr_{0.95}Pr_{0.05})TiO_3$, unlike insulating $SrTiO_3$, is a degenerate semiconductor, which also complicates the situation. In conclusion, 2DEG did not form in [100] due to electron gas that was not localized enough or its formation was of a minor nature for a clear identification.
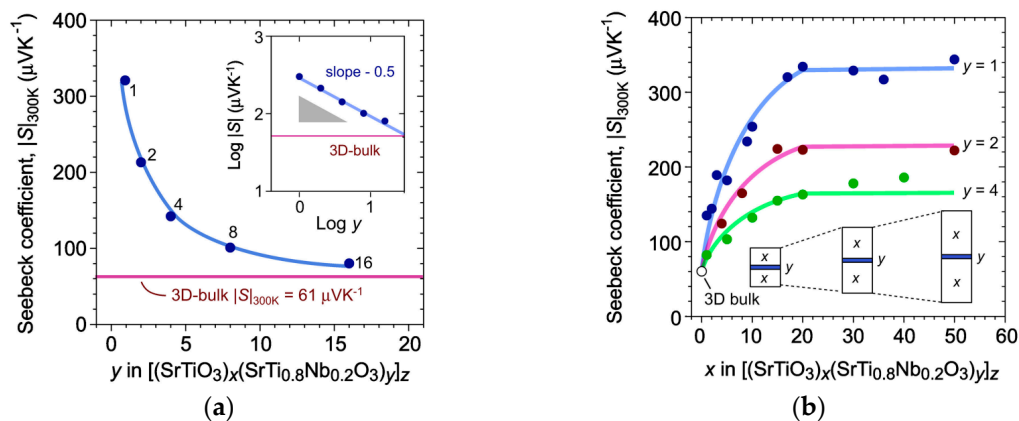

Figure 5. Thermo-emf dependence of $Sr(Ti_{0.8}Nb_{0.2})O_3$ of layer at 300 K for $[SrTiO_3]_x/[Sr(Ti_{0.8}Nb_{0.2})O_3]_y$ superlattice: (**a**) On y (thickness of the conducting layer) at sufficient thickness of insulating layers; (**b**) on x (thickness of insulating layers) at sufficient thickness of conducting layers. Reproduced from [101].

Unfortunately, the series of works [27,101,102] did not provide direct thermal and electric conductivity measurements. The *ZT* value was assessed via evaluation at 300 K using Seebeck's coefficient S, thermal conductivity for $SrTiO_3$ single crystal, and conductivity σ calculated from Equation (14) with the measured charge carriers concentration and reference data on their mobility. The *ZT* value for 2DEG at 300 K was found to be 2.4—that is extremely large. Mean *ZT* for the superlattice was 0.24, which is nearly twice as large than the *ZT* value (0.11 at 300 K) for superlattice (8,8) from [100]. This mainly proves the advantage of the 2DEG-based strategy for the $SrTiO_3$-containing systems over the conventional doping and over the simple combination of differently alloyed thermoelectric materials.

The paper [27] also studied the properties of a $TiO_2/SrTiO_3$ hetero interface formed on the boundary of a 56 nm TiO_2 layer and a 0.5 mm $SrTiO_3$ layer. For that system, the depth profile of carrier concentration was obtained. There is a peak observed in the region of ~0.3 nm-thick of TiO_2 side in the heterointerface, which exceeds by 2–2.5 orders of the magnitude the charge carriers concentration in the bulk of TiO_2. This clearly proves the spontaneous 2DEG formation on the heterointerface of such oxides due to the reasons described in the previous section. Thermo-emf *S* and conductivity σ were measured for the $TiO_2/SrTiO_3$ heterointerface, $SrTiO_3$ after mechanical removal of TiO_2 layer, and for a separate 126 nm-thick TiO_2 layer [27]. Thermo-emf *S* of $TiO_2/SrTiO_3$ was shown to be 1050 $\mu V/K$ at 300 K and is caused mainly by the presence of heterointerface. Unfortunately, any assessments of the *ZT* value for that heterointerface were absent.

Based on results from [27,101,102], papers [10,11,69] presented the design of a hypothetic material, which can efficiently utilize 2DEG properties, and modelling the properties of such material. It was proposed to fabricate the $SrTiO_3$-based material doped with ions in both sublattices. Particularly, grains of $(Sr,La)TiO_3$ containing 2–7 at.% of La^{3+} in the positions of Sr^{2+} are supposed to be separated by thin layers (called "grain boundaries" in these papers) of $Sr(Ti,Nb)O_3$ containing 20 at.% of Nb^{3+} in the Ti^{3+} positions. Both scenarios of substitution lead to free electrons occurring in the structure, while charge compensation is provided by oxidation state change of titanium from +4 to +3 ($Ti^{4+} + e^- \rightarrow$

Ti^{3+}). Substituting Ti with Nb leads to decrease of the conduction band edge, while Sr substitution with La has no effect on it, thus, causing 2DEG formation on the grain boundaries [10,11,69,99].

In the suggested system, grains are in cubic modification [10,11,69]. Therefore, the whole system is a superposition of three $[(Sr_{1-a}La_a)TiO_3]_x/[Sr(Ti_{0.8}Nb_{0.2})O_3]_y$ superlattices along three mutually perpendicular dimensions (Figure 6). The superlattice itself along one of the dimensions can be considered as an analogue to the superlattices studied in [27,101,102], while the La doping controls the total electron concentration in the system. That is why, the size of cubic grains in papers [10,11,69] was chosen to be 16 unit cells (x = 16) in accordance with [27,101,102]. On one hand, such geometry is necessary to prevent the collapse of electron confinement, but on the other, to maximize 2DEG concentrated on the boundaries with respect to the total volume of the system. Thickness of well-conducting Nd-doped grain boundaries ranged from 1 to 16 unit cells.
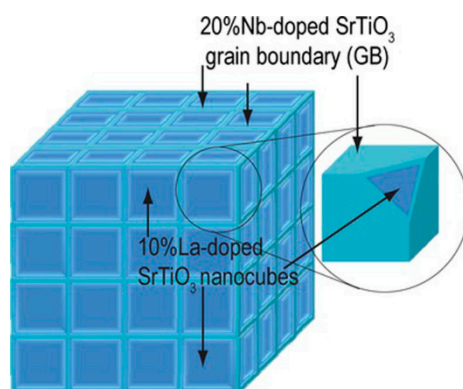

Figure 6. "Rubik's cube" structure of the $SrTiO_3$ ceramics (2DEG grain boundaries are shown in light blue, grain interiors—in deep blue). Reproduced with permission from Reference [11].

When calculating thermoelectric characteristics of the material (Figure 6), the authors in [10,11,69] used thermoelectric properties of the boundaries from [27,101,102], while thermoelectric properties of grains were modelled given 2DEG occurs on their boundaries. For electrons in the bulk of grains, 2DEG was considered as a charged shell acting as a potential barrier for free electron motion in the material's bulk or, in another words, it behaves as an "electron filter" (See Section 3). The *ZT* value for such material with minimal thickness of $Sr(Ti_{0.8}Nb_{0.2})O_3$ boundaries (1 unit cell) was shown to be ~0.8–1.2 at 300 K depending on the height of potential barrier created by 2DEG.

Some criticism on the works [10,11,69] is provided in Section 5. After all, the results by K. Koumoto et al. clearly demonstrate the nanostructuring as the key approach to drastic improvement of the oxide's thermoelectric characteristics.

5. $SrTiO_3$-based Biphase Ceramics

5.1. Some Experience on Manufacturing of the "Biphase" Thermoelectric Materials

Epitaxial growth of superlattices or their fabrication by other methods enabling precise phase arrangement, all these techniques are "lab-scale" and not suitable for large-scale production. Even for epitaxial methods, the fabrication of a non-planar 3D superlattice similar to the on discussed in [69] is challenging. This suggests to us to turn an eye on less "sophisticated" approaches of materials engineering with the corresponding experimental results being discussed below.

Primarily, let us pay attention to the papers [103,104], which studied the fabrication of La-doped $SrTiO_3$ nanocubes with Nb-doped surface. It may be considered as an attempt to prepare structures of the type investigated in [69]. Such nanocubes were synthesized via a rapid synthesis combining a rapid sol-precipitation and hydrothermal process. The La-doped $SrTiO_3$ nanocubes were formed at room temperature by a rapid dissolution of NaOH pellets during the rapid sol-precipitation process, and the Nb-doped surface (shell) along with Nb-rich edges formed on the core nanocubes via the

hydrothermal process. Size of the obtained cubes ranges from 80 to 150 nm [104] with the thickness of Nb-doped layer being 3–4 nm [103]. The paper [104] also features self-assembling of such "cells" at slow drying on SiO_2/Si support. Cubes tend to form dense packed face-to-face clusters forming a continuous smooth layer of 10 μm thickness. Unfortunately, the consolidation of such a system was not studied.

The best characteristics in the theoretical paper [69] was found for a structure with the following properties: Boundary thickness of 1 unit cell (~0.3 nm) to form high density 2DEG; grain size of 16 unit cells (~6.5 nm) to prevent tunneling of electrons localized on grain boundaries as 2DEG. This is in agreement with earlier results presented in [102]. It is noteworthy that thickness of Nb-doped surface of La-doped $SrTiO_3$ nanocubes is very high [103,104]. Even at ideal consolidation two such cubes form compound Nb-doped layer ~7 nm thick that is already large and leads to complete 2DEG failure [102]. Size of such nanocubes is, of course, high enough to isolate reliably the intergranular layers from each other. However, at that size the contribution of intergranular phase to the total thermoelectric characteristics appears to be rather small, even in case of its thickness small enough for 2DEG formation. Thus, nanocube system presented in [103,104] can provide only an advantage of electron filtration. Apparently, further technological advances towards fabrication of such cubes will finally allow obtaining small enough La-doped $SrTiO_3$ nanocubes with rather thin Nb-doped surface to implement hypothetical system presented in [69].

Another attempt to implement hypothetical nanostructured material from [69] is described in [105], where design of La-doped $SrTiO_3$ grains with Nb-doped surface was done via an alternative route. As a starting material the commercial 5 at.% La-doped $SrTiO_3$ (Titan Kogyo Co., Tokyo, Japan) was used. Surface layer of NbO_x was formed on powder particles via adding $Nb(OEt)_5$ oxalic acid aqueous solution followed by filtration and drying. Modified and unmodified powders were sintered using spark plasma sintering at 950 °C in ~3 min at 200 MPa. Sintering yielded in fine-grained ceramics containing dense-packed particles with identical size distribution ranging in 200–500 nm. This work demonstrated two main features, namely, NbO_x does not form separate phase of non-perovskite type but is chemically bound to main $SrTiO_3$ material. Additionally, Nb localization in the system has been addressed.

Nb concentration in Ti positions was found to be 1.3 ± 0.4 at.% [105]. It was demonstrated that unlike doping with additional element and fairly close charge carrier concentrations, modified sample is a worse conductor than unmodified one. The authors explains this result with space localization of Nb along grain boundaries.

Substitution of Ti with Nb in $SrTiO_3$ decreases conduction band edge [105]. Thus, there is formed a zone of potential minimum for electrons along the boundaries and charge concentrating occurs. Charged grain boundaries play a role of potential barrier for conduction band electrons, acting as an electron filter in accordance with concepts from [69]. Such concepts do fit well to explain lower conductivity of the modified sample (part of the electrons does not pass through the potential barrier on the grain boundaries) as well as higher thermo-emf (electron filter in Equation (15)) and power factor. Unfortunately, space localization of Nb or charge on the boundary were not found directly in [105]. Meanwhile, thickness of conductive layer even at 6–7 nm completely violates electron confinement with 2DEG state being collapsed [102]. Additionally, grain size of ceramics obtained in [105] ranges from 100 to 600 nm, which is too large to observe any valuable contribution of 2DEG to thermoelectric properties of the material, as indicated by authors.

According to theoretical paper [69], at optimal barrier height the power factor of the main material (without taking into account thermoelectric characteristics of the boundaries) can increase by ~36%. Power factor was observed to increase by the same order of magnitude in paper [105] (~35%) when modified and unmodified ceramics were compared at optimal conditions (450 K). This is the strongest argument for Nb and charge localization along the boundaries. However, there is no reasons to suppose that electrons near the boundaries are in the 2DEG state. On the one hand, thickness of NbO_x layer applied on the powder particles is unknown, on the other hand, thermal diffusion during sintering may have led to Nb-rich zone, too wide for 2DEG formation, while properties enhancement

occurred due to electron filtration and increased total number of electrons in the system. Additionally, the authors in [105] did not consider influence of heterophase boundaries between the grains on thermal conductivity. Obviously, such boundaries may efficiently dissipate phonons that contributes to reduction of thermal conductivity and increases the *ZT* value.

It can be temporary summarized that purely ceramics approach for systems with electrons concentrated along grain boundaries is one of the most prospective. The key problem towards its successful application consists in creating an electron-scavenging layer. That is why, in our opinion, it is reasonable to shift towards biphase ceramics, in which 2DEG is spontaneously formed on the boundary between two phases. Some variants of heterointerfaces providing 2DEG have already been discussed earlier here. Let us consider some complications regarding preparation of such structures in the form of ceramics in more detail.

Sintering of biphase ceramics from two structurally close materials can involve mutual thermal diffusion of the elements. It easy to demonstrate for the grain boundaries of $SrTiO_3/GdTiO_3$. Heterointerface itself can be considered as Gd-doped $SrTiO_3$ layer of 1 unit cell thickness. Because $SrTiO_3$ is easily doped with Gd [61], the problem of single-phase formation is rather topical here. But even for that case thermal diffusion at sintering may initiate Gd doping of $SrTiO_3$ grains surface. This will yield in spreading Gd-doped layer, expanding the region of electron gas localization, and, as a result, collapsing 2DEG. Paper [75] showed for $GdTiO_3/SrTiO_3$ layers grown by molecular beam epitaxy that electron gas density reduces by 20% after the introduction of Sr ions. However, at Sr concentration >4 at.%, $Gd_{1-x}Sr_xTiO_3$ undergoes insulator-to-metal transition, which is a feature of rare earth titanates [106]. Therefore, surface alloying of $GdTiO_3$ ceramics grains by Sr at thermal diffusion may also lead to expansion of electron gas localization area and 2DEG collapse.

Thus, mutual atom diffusion at sintering of structurally close compounds may give a rise to a number of complications yielding a 2DEG collapse due to delocalization of conduction band along grain boundaries. That is why we suggest to utilize the effect of spontaneous 2DEG formation on the interface of two different phases, e.g., $TiO_2/SrTiO_3$ [27]. TiO_2 and $SrTiO_3$ will hardly form single phase, while 2DEG is obtained on their heterointerface because of modulation alloying owing to difference in conduction band edge [98], which is hardly affected by La-doping [99]. That is why, even mutual exchange of alloying elements may unlikely lead to collapse of 2DEG state. Thus, unlike theoretical paper [69], we suggest a biphase structure composed of TiO_2 and $SrTiO_3$ grains (Figure 7). The dashed area shows 2DEG localization from the TiO_2 side in the interface. Relative scale corresponds to 1 unit cell of TiO_2 localizing 2DEG and to 16 unit cells of TiO_2, which are necessary to prevent electron tunneling (Figure 7).
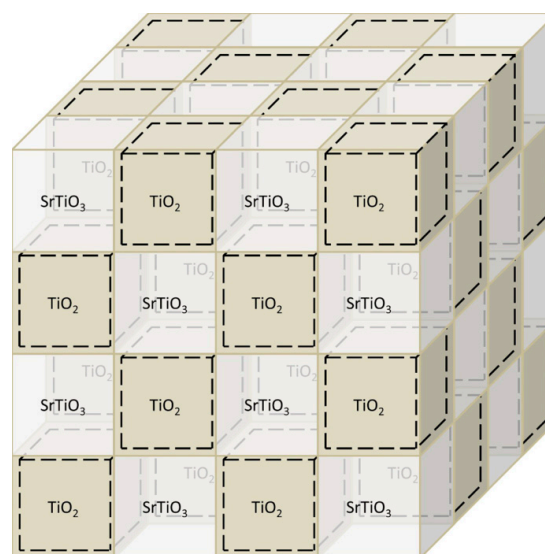

Figure 7. Ideal structure of $TiO_2-SrTiO_3$ biphase ceramics.

As was mentioned above, the *ZT* value of the hypothetic model $SrTiO_3$-based material utilizing 2DEG properties at most reaches 0.8–1.2 at 300 °C at minimal thickness of separating layer and small grain size [69]. These factors enable one to expect drastic improvements of thermoelectric properties of the suggested TiO_2–$SrTiO_3$ biphase ceramics (Figure 7). It is worth mentioning again that electron tunneling through the thin (1 unit cell) charged edge with 2DEG was not taken into account in [69]. For real systems, this may lower the effect of electron filtration and reduce thermoelectric efficiency.

On the other hand, structure of real ceramic systems will be quite different from the ideal model (Figure 7). However, if TiO_2 and $SrTiO_3$ grains are in checkered order in the bulk, then 2DEG localized on the heterointerface of these phases will form the integrated network along the surface between the grains permeating throughout the whole material.

The density of a real 2DEG network can be lower than in the ideal system, because grain shape in perovskite ceramics is usually a truncated cube rather than ideal cube as considered in the model. Anyway, grain size plays the major role and is hard to retain within the range found for the ideal system. Another hurdle is the fabrication of highly dense ceramics with minimal variance of grain size, i.e., it is undesirable to obtain lower grain sizes than is required to separate reliably different 2DEG regions from each other and to prevent 2DEG collapse. At this regions, 2DEG may be partially or completely collapsed leading to decline in performance of the whole 2DEG network. Also, small grain size is not only necessary for increasing of 2DEG contribution to the thermoelectric characteristics of the material. Transfer from coarse-grained to fine-grained ceramics allows the improvement of the physico-chemical properties of the material (hardness, fracture viscosity, ductility and etc.) due to significant contribution of intergranular boundaries states [107]. Fabrication of highly-dense biphase ceramics and its challenges will be discussed in the next section.

Another important feature in the real ceramics system is the additional loss of electron energy in 2DEG network at the curved places of connection between separate 2DEG regions on the grain boundaries. 2DEG transport along the grain boundaries is similar to transport in superlattice within the context of ideal system, because various 2DEG planes in the network are mutually orthogonal [69]. However, in real system separate 2DEG surfaces on grain boundaries may be curved and are arranged chaotically to each other. That is why it is impossible to choose some direction, along which the network would perform the same as the superlattice. Meanwhile, it was shown for the similar problem of electron motion in deformed graphene layer that in the curved places additional dissipation of motion energy occurs [108,109]. Similar processes should also take place in the 2DEG network of the real ceramics that can have a negative impact on its thermoelectric properties as compared to an ideal system.

Indicated issues clearly show that *ZT* values reported in [69] for an ideal system are rather overestimated. But in general, TiO_2–$SrTiO_3$ biphase ceramics with ordered 2D surface along grain boundaries should be characterized by enhanced thermoelectric properties due to 2DEG formation on this surface.

Let us consider experimental work devoted to $SrTiO_3$-based ceramics with the addition of TiO_2 [110]. Single-phase Nb-doped submicron powder of strontium titanate $Sr(Ti_{0.85}Nb_{0.15})O_3$ was prepared via solid phase synthesis from highly pure powders of $SrCO_3$, TiO_2, and Nb_2O_5 in argon atmosphere at 1400 °C for 4 h. Additional surface modification of the powder particles with nanosized particles of TiO_2 was performed by liquid phase precipitation of $(NH_4)_2TiF_6$ (0.06 M) and H_3BO_3 (0.2 M) in the water solution for 2 h at room temperature [111]. Pressed at 20 MPa samples of modified and nonmodified powders were being sintered in graphite crucible in argon atmosphere at 1500 °C for 3 h. Porous ceramics samples were obtained (Figure 8) with significantly different thermoelectric properties (Figure 9).
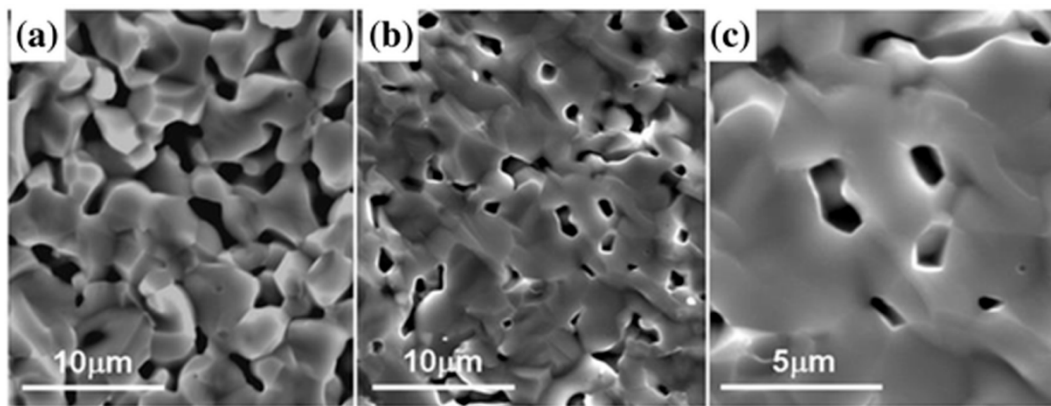
Figure 8. SEM images of Nb−SrTiO₃ ceramics (**a**) with and (**b**,**c**) without the surface modification of nanosized titania. © 2016 Li E, Wang N, He H, Chen H. Published in [110] under CC BY 4.0 license. Available from: https://doi.org/10.1186/s11671-016-1407-8.
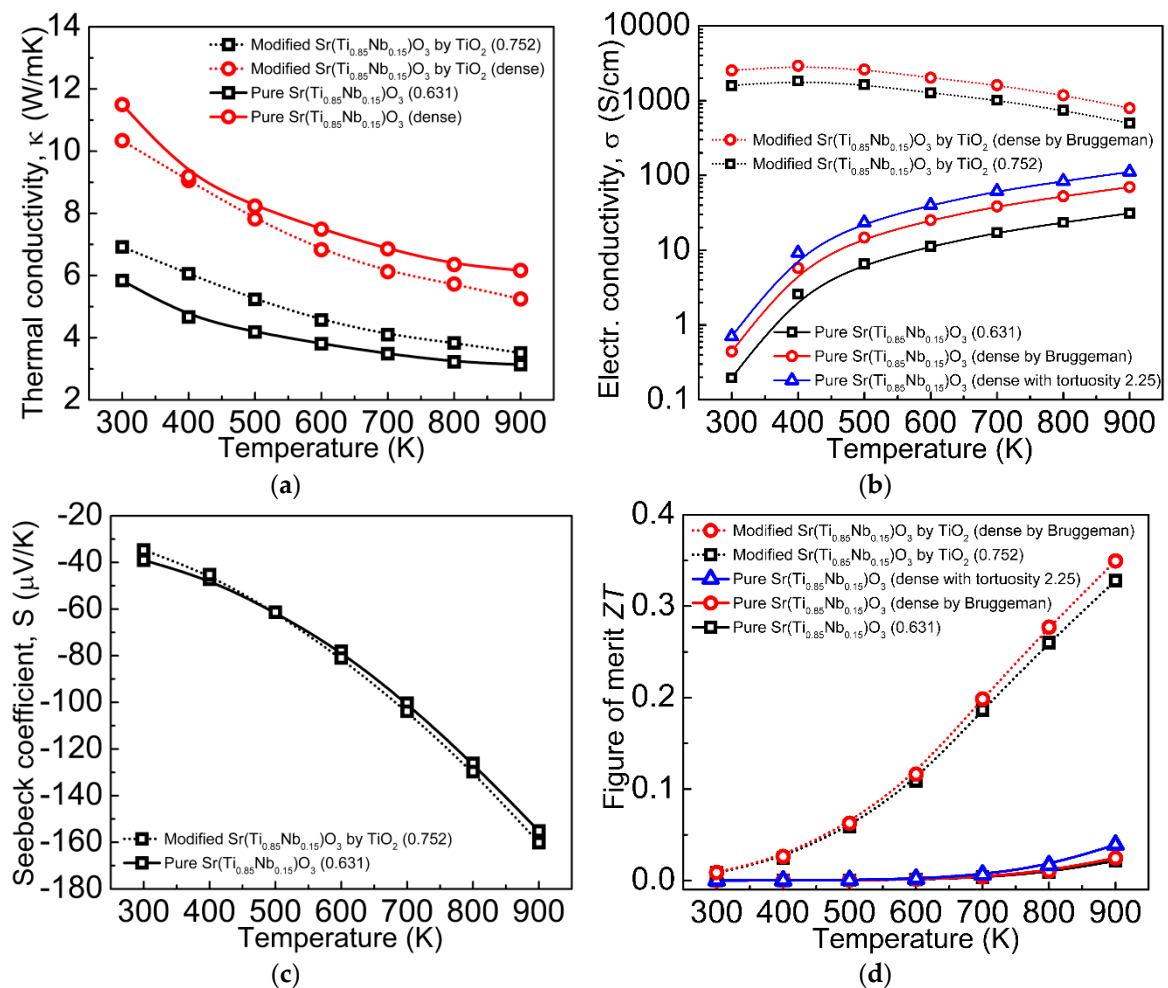
Figure 9. Temperature-dependent thermoelectric properties of Nb−SrTiO₃ ceramics obtained from submicron Sr(Ti$_{0.85}$Nb$_{0.15}$)O₃ powder either modified or non-modified with TiO₂: (**a**) Thermal conductivity; (**b**) Electrical conductivity; (**c**) Seebeck coefficient; (**d**) Figure of merit *ZT*. © 2016 Li E, Wang N, He H, Chen H. Published in [110] under CC BY 4.0 license. Available from https://doi.org/10.1186/s11671-016-1407-8.

Because obtained thermoelectric materials are porous, the influence of porosity on thermoelectric properties should be addressed. Thermal conductivity of such media is usually described by P.G. Klemens (Equation (16)) [112]:

$$\kappa_{eff} = \kappa_o(1 - 4p/3),\tag{16}$$

where κ_{eff}—effective thermal conductivity of the porous medium; κ_o—thermal conductivity of the full dense material; ρ—porosity.

Relative density of the original and titania-modified Nb−SrTiO$_3$ samples are 63.1% and 75.2%, respectively. Due to the different porosity of the materials, the paper [110] compared their thermal conductivity with recounting according to P.G. Klemens' Equation (16): Thermal conductivity of more porous nonmodified Nb−SrTiO$_3$ sample was recounted at density of less porous titania-modified one. At the same time, Figure 9a shows thermal conductivity recounted by us in accordance with Equation (16) for full dense modified and nonmodified materials. As can be seen, surface modification of strontium titanate Sr(Ti$_{0.85}$Nb$_{0.15}$)O$_3$ powder particles with titania greatly reduces thermal conductivity. Given the grain size for both ceramics is the same (order of few microns, Figure 8) and TiO$_2$ content is small (not provided, but it can be concluded from the synthesis routine [110]), thermal conductivity reduction should be caused by high phonon dissipation on the heterophase interfaces. Additionally, this again proves the prospects of thermoelectrics based on TiO$_2$−SrTiO$_3$ biphase ceramics.

Conductivity of the two samples is also rather different (Figure 9b). The work [110] just notes surface modification of Sr(Ti$_{0.85}$Nb$_{0.15}$)O$_3$ powder particles with titania drastically increases conductivity. The effect of porosity is not considered as in the case of thermal conductivity. The same problem of porosity effect on conductivity of oxide ceramics was studied in [113]. Although this paper [113] reported on the conductivity of nondegenerate insulator La$_2$Mo$_{1.5}$W$_{0.5}$O$_9$, while SrTi$_{0.85}$Nb$_{0.15}$O$_3$ is a degenerate one in this case, approaches suggested they are of universal nature.

For biphase media, where one phase is incapsulated into the other one as spherical inclusions, authors in [113] suggest to use two models of conductivity: Maxwell−Garnett [114,115] and Bruggeman [116,117]. These models assume the conductivity of the incapsulated medium to be zero that corresponds to pores. There are Equations (17) and (18) in [113]:

$$\sigma_{eff} = \sigma_0\frac{1 - p}{1 + p/2},\tag{17}$$

$$\sigma_{eff} = \sigma_0\frac{2 - 3p}{2},\tag{18}$$

where σ_{eff}—effective conductivity of the porous material; σ_o—conductivity of the full dense material.

Equation (17) based on the Maxwell−Garnett model is valid till porosity 0.135, therefore, it is not applicable to materials from [110]. Equation (18) based on the Bruggeman model is valid till porosity values up to 0.22, although it was shown to be applicable till ~0.28 [113]. That is why we used Equation (18) to evaluate conductivity of full dense material from the data on more dense material obtained via surface modification of Sr(Ti$_{0.85}$Nb$_{0.15}$)O$_3$ with titania [110]. A less dense sample obtained from powder without surface modification was also subjected to analysis. It was shown to implement tortuosity factor τ [118] for conductivity assessment of highly porous materials [113] in order to take into account complex geometry of porous channels (Equation (19)):

$$\sigma_{eff} = \sigma_0\frac{1 - p}{\tau}\tag{19}$$

To determine tortuosity one needs more extensive experimental data like the one presented in [113]. Particularly, for highly porous system with porosity P = 0.34 the tortuosity was found to be 2.25 [113]. Given this, we used tortuosity τ = 2.25 for more correct assessment of conductivity of less dense material (Equation (19)) obtained from Sr(Ti$_{0.85}$Nb$_{0.15}$)O$_3$ without modification with titania [110].

We did not take into account pore geometry, which can be different for the ceramics studied in [110] and [113].

Figure 9b provides conductivity values calculated using Equations (18) and (19) for full dense materials, modified and nonmodified ones. As can be seen, addressing porosity shortens the difference in conductivity between the materials a bit, although the gap is still of several orders of magnitude.

Temperature characteristics of Seebeck's coefficient *S* for both materials are very close [110] (Figure 9c). Effect of porosity on *S* still remains unclear [119]. On one hand, pores are equivalent to removing a part of thermoelectric material from the volume, therefore, it should proportionally reduce the *S* value. On the other hand, pores may act as dissipation sites for low electrons [120], performing as electron filters and having a positive impact on the *S* value. In general, temperature dependence data on *S* from [110] is close to the one obtained for dense $Sr(Ti_{0.8}Nb_{0.2})O_3$ ceramics from [121] (Figure 9c).

The paper [110] reported *ZT* values calculated for the data without addressing porosity and it turned out to be drastically different for $Sr(Ti_{0.85}Nb_{0.15})O_3$ ceramics and for the one modified with titania (Figure 9d). We have done revision using corrected values, but it did not make much difference for temperature dependence of the *ZT* value (Figure 9d). Apparently, corrections for thermal and electrical conductivity are of the same order and compensate each other at evaluation of the *ZT* value, because $ZT \sim \sigma/\kappa$. Temperature dependence of *ZT* value for titania-modifed $Sr(Ti_{0.85}Nb_{0.15})O_3$ is close to the one evaluated for $Sr(Ti_{0.8}Nb_{0.2})O_3$ ceramics [121].

Unfortunately, the work [110] did not study spatial distribution of titania to reveal exact mechanisms of its influence. The grain size of TiO_2 is too high (few microns) for 2DEG formed on heterointerface to contribute much to thermoelectric properties. Absence of data on TiO_2 phase localization does not allow any conclusion on possible formation of an ordered 2DEG network in the composite material. Main difference in *ZT* values is caused by drastically different conductivity of the obtained materials. Possible reasons to this suggested by the authors in [110] are: Better conditions for ceramic grain growth as a result of surface modification with titania; possible contribution of the formed titanium carbide phase that is a better conductor than the oxides in the studied system. Also, there may be a contribution from 2DEG, which is likely formed on the heterointerface. In general, thermoelectric characteristics of TiO_2-modified ceramics based on $Sr(Ti_{0.85}Nb_{0.15})O_3$ are close to the dense one $Sr(Ti_{0.8}Nb_{0.2})O_3$ [121]. TiO_2 in that case plays a role of sintering additive. Abnormally low conductivity of the starting porous $Sr(Ti_{0.85}Nb_{0.15})O_3$ ceramics remains unclear, because it stays low in comparison with dense ceramics from [121] even after accounting for porosity in terms of dense ceramics. Summarizing the results of work [110], $Sr(Ti_{0.85}Nb_{0.15})O_3$-based composite ceramics modified with TiO_2 is way too different in terms of structure compared to the biphase ceramics system we are suggesting (Figure 7). At least, the work [110] clearly demonstrates a positive influence of heterointerfaces (Figure 9) on thermal conductivity with the latter being considerably reduced.

Finally, one should pay attention to possible phase transition of titania (anatase–rutile) during sintering. 2DEG formation on $TiO_2/SrTiO_3$ heterointerface was considered here for the TiO_2 anatase phase. However, formation of highly dense $TiO_2−SrTiO_3$ biphase ceramics requires sintering temperatures above 1000 °C. In 1967, A. Navrotsky and O. J. Kleppa observed phase transition anatase-rutile at 1050 °C when heating commercial anatase for 16 h [122]. Complete transition to rutile from anatase was demonstrated for ceramics sintering at 1100–1350 °C for 6 h [123] and at 1500 °C for 10 h [124]. Although here we suggest obtaining $TiO_2−SrTiO_3$ ceramics using spark plasma sintering, which implies by an order of magnitude shorter sintering durations, nevertheless, rutile formation is inevitable. In the next section, we will show that despite the conduction band edge of rutile being higher than that of anatase, strontium titanate is characterized by a higher conduction band edge anyway, which is the main factor for 2DEG formation on the heterointerface. Thus, possible rutile formation does not change the synthesis scheme of $TiO_2−SrTiO_3$ biphase ceramics, which intergranular boundary provides an ordered 2DEG network.

5.2. Quantum Chemical Analysis of TiO₂/SrTiO₃ Heterointerface Structure

According to TEM of epitaxial films of pure anatase TiO_2 on undoped and *n*-type $SrTiO_3$ [125,126], the most stable from an electrostatic standpoint is the structure of interface boundary given on Figure 10. However, this data does not provide enough information on heterointerface structure, e.g., about the edge of $SrTiO_3$ support and how it is integrated with TiO_2 film. That is why quantum chemical calculations is an important tool for studying electron structure of the heterointerface and how it correlates with thermoelectric properties.
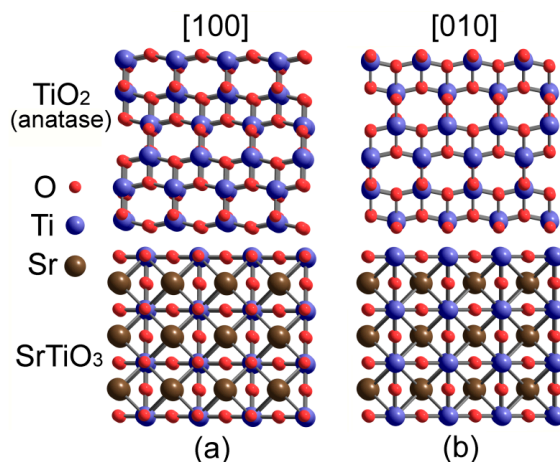

Figure 10. Structure of the heterointerface anatase TiO_2 (001) on $SrTiO_3$ (001) according to TEM image [125,126]. The views are along (**a**) the [100] and (b) the [010] directions.

Electronic structure of solids is frequently simulated via methods of density functional theory (DFT) [127,128], which are commonly applied with Khon–Sham formalism [129] using local density or the generalized gradient approximations (LDA and GGA, respectively) for the exchange-correlation functional. Modern DFT calculations often involve the projector augmented-wave (PAW) method [130,131], which combines simplicity of first-principles pseudopotential [132] and accuracy of linearized augmented planewave method [133]. PAW is an all-electron technique, which enables one to determine potential using all-electron density. That is why PAW proved to be as one of the most robust approximations for electronic structure modelling of crystals. Additionally, electronic structure of metal oxides is successfully simulated by the DFT+U technique, which was originally suggested [134] as a continuation of LDA within the Hubbard model [135]. As compared to hybrid functionals and resource-intensive post-Harthree–Fock methods (configurational interaction, Moller–Plesset perturbation theory, GW approximation and etc.), the DFT(LDA/GGA)+U approach provides equally correct results at fairly low computational cost. When optimal value of $U = U_o - J$ are chosen (where U_0 and J specifies the Coulomb and exchange interaction parameters, respectively [136]), one can obtain correct data on the electronic structure of solids as well as assess atomization potentials and energy of intermolecular interactions [137]. Simulations combined with the U correction can well describe the physical properties of periodic systems like magnetic and structural properties of correlated systems, the electron transfer energetics, and chemical reactions. The relative success of the DFT+U method owes its direct approach to accounting for the underestimated electronic interactions by the simple addition of a semiempirically tuned numeric parameter "U" [138] that can be easily controlled. This makes the DFT+U method a convenient tool to qualitatively assess the influence of electronic effects on physical properties of perovskites [139].

To reduce self-interaction error, in comparison to LDA and GGA, A.D. Becke suggested including a part of Hartree–Fock exchange energy into the ʙexchange functional [140] that had led to a great number of hybrid potentials, e.g., B3LYP [141] and PBE0 [142]. After implementation of plane wave codes [143] it became possible to use hybrid functionals for simulations of solid's electronic structure

that provided more accurate results (as compared to GGA) on lattice constants, atomization potentials, tensile energies and etc. However, to assess the Hartree–Fock exchange under periodic boundary conditions using plane waves one needs twice as many computational resources as compared to GGA.

DFT/PAW modelling using the GGA PW91 functional [144] was used to study the atomic structure of the interface between $SrTiO_3$ substrate and anatase TiO_2 thin films [145] with results being in agreement with transmission electron and high-angle annular-dark-field microscopy data. Out of 24 possible interfacial geometries the most stable heterointerface structures were chosen, which were analyzed in terms of electron density distribution. Calculations by Z. Wang et al. have shown that the interface boundary contains SrO-terminated $SrTiO_3$ and Ti-terminated TiO_2, while the interfacial Ti atom from TiO_2 is located above the hollow site (Figure 11) that is found to be the most energetically preferred. Besides, the modelling predicted mixed ion-covalent bonds in the $TiO_2/SrTiO_3$ interface as well as notable rearrangement of oxygen sublattice in the heterointerface. Namely, interfacial oxygen atoms of TiO_2 are pulled towards the SrO plane of the $SrTiO_3$, flattening the original zigzag of the TiO_2 atomic chain.
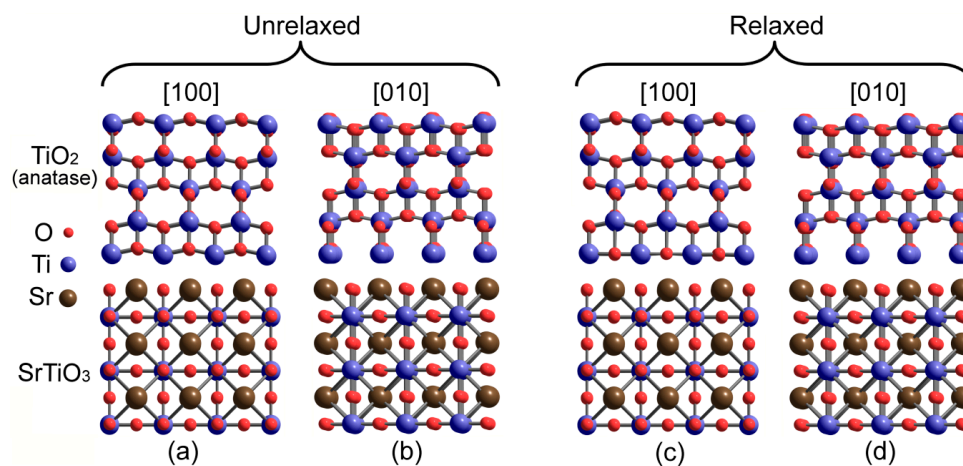

Figure 11. Structures of (**a**,**b**) unrelaxed and (**c**,**d**) relaxed interfaces between the SrO-terminated $SrTiO_3$ and the Ti-terminated TiO_2 according to [145]. Interface titanium atoms of TiO_2 are located above hollow sites of $SrTiO_3$ surface. The views are along (**a**,**c**) the [100] and (**b**,**d**) the [010] directions.

Theoretical investigations of the $TiO_2/SrTiO_3$ heterointerface presented above are carried out for anatase modification of titania. However, TiO_2 grain structure in the biphase TiO_2–$SrTiO_3$ ceramics may correspond to rutile modification (See Section 5.1). That is why it is necessary to consider 2DEG formation on the TiO_2(rutile)/$SrTiO_3$ interfacial boundary. In accordance with the results of DFT/PAW simulations using three GGA exchange-correlation functionals for three potential epitaxial orientations between TiO_2 and $SrTiO_3$, the bond is observed only for the interface rutile TiO_2 (001) on $SrTiO_3$ (111) [146]. Experimental results from [98,147] show that conduction band edge of $SrTiO_3$ is higher by 0.40 and 0.20 eV than that of anatase and rutile, respectively (Figure 12).

Namely, there is an opportunity to obtain 2DEG (modulation doping) on the boundary between thin films of rutile TiO_2 (001) and $SrTiO_3$ (111) that is also true for interface with anatase TiO_2 (see Section 4.1). At the same time, modelling atomic and electronic structure of the interface rutile TiO_2 (001) on $SrTiO_3$ (111), according to [145], will enable us to obtain important results on structure of $SrTiO_3/TiO_2$ (rutile) heterointerface with various alloying agent to $SrTiO_3$ and/or TiO_2.

Regarding the preparation of fine-grained thermoelectric ceramics, one may also need calculations of the molecular structure of interacting nanoparticles to interpret experimental data. For example, the paper [148] reported the investigation of molecular structure of spherical TiO_2 nanoparticles of various sizes (from 300 to 1000 atoms) using self-consistent charge density functional tight-binding (SCC-DFTB) and DFT (B3LYP). From an electronic structure standpoint, the accuracy of the bandgap

energy calculations was assessed (Table 1). SCC-DFTB approximation was shown to provide rather accurate geometry and electronic structure of real sized TiO_2 nanospheres (up to 4.4 nm).
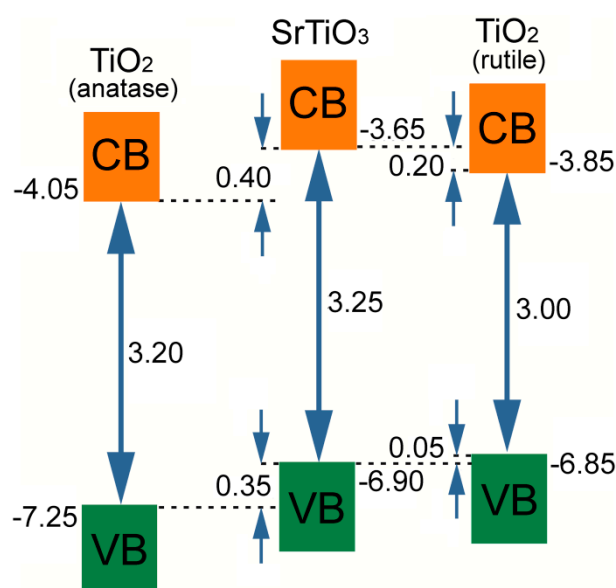

Figure 12. Energy level diagram (eV) of anatase, rutile, and $SrTiO_3$ nanoparticles according to [98,147]. CB and VB stand for conduction band and valence band, respectively.

Table 1. Electronic band gap for bulk anatase TiO_2. Self-consistent charge density functional tight-binding (SCC-DFTB) values have been compared to the experimental data, values calculated with standard GGA-DFT, with hybrid DFT functionals, GGA-DFT Hubbard corrected and post-Hartree–Fock GW approximation [149].

Method	PBE	PBE0	B3LYP	PBE+U	GW	DFTB	Experiment
Band gap, eV	2.36 [150]	4.50 [151]	3.81 [152]	3.27 [151]	3.83 [153]	3.22 [148]	3.4 [154]

Being in good agreement with the results of GW approximation, SCC-DFTB was successfully used to investigate the effects of ferroelectric domain walls on electronic transport properties and charge carrier recombination in organometallic halide perovskites [155]. Besides, the SCC-DFTB method was demonstrated to be reliable for a variety of TiO_2 modifications [156,157]. Namely, SCC-DFTB modelling molecular structure of interacting nanoparticles of TiO_2 and $SrTiO_3$ as well as simulating their grain structure with alloying agent will enable to predict their optimal size and type/quantity of the agent, respectively. This is an indispensable step towards targeted engineering of TiO_2–$SrTiO_3$ ceramic thermoelectrics with maximal *ZT* value.

5.3. TiO$_2$–SrTiO$_3$ Biphase Nanoceramics: SPS Approach

As was mentioned earlier, consolidation (sintering) methods gain specific importance when it comes to fabrication of nanostructured thermoelectrics. On the one hand, it is necessary to obtain highly-dense material, on the other hand, preserving small (nanoscale) grain size is crucial. Such material's microstructure is important to improve its electrical conductivity and reduce thermal conductivity that is desired for thermoelectric applications. A variety of sintering techniques have been used in the literature to achieve $SrTiO_3$-based bulk samples. However, hot pressing (HP) and spark plasma sintering (SPS) are the most commonly used techniques for making high-density (typically >95% of the theoretical density) and small crystal size (<1 μm) $SrTiO_3$-based bulk samples (Table 2). Accordingly to Table 2, the maximum dimensionless figure of merit obtained by A. Kikuchi et al. in SPSed 8 at.% La-doped $SrTiO_3$ (*ZT* = 0.37 at 1045 K) [158], and by Y. Wang et al. in HPed 5 at.% Gd-doped $SrO(SrTiO_3)_2$ (*ZT* = 0.24 at 1000 K) [159].

The concept of SPS (rapid heating under pressure with pulses of direct current) consists in rapid heating of nanopowders to sintering temperature at a high speed (to 250 °C/min) by short (order of ms) electric pulses under moderate pressure (<100 MPa). Such conditions favor grain-boundary and surface diffusion, i.e., densification dominates over grain growth. Short sintering cycle provides ceramics with submicron- and nano-grained structure with a density close to theoretical. Owing to high pulse frequency, total amount of energy transferred by spark discharges is comparable with energy transferred in the graphite die that provides uniform heating of the material yielding a uniform composition of the obtained product [160].

Table 2. Lists the hot pressing (HP) and spark plasma sintering (SPS) parameters employed to prepare $SrTiO_3$-based ceramics reported in the literature by several groups.

	Authors	Composition	Sintering Conditions	Pressure	Density	Largest Figure of Merit	Ref.
1	H. Obara et al.	10 at.% Y-doped $SrTiO_3$	HP @ 1400 °C, 1 h	100 MPa (Argon)	>97%	ZT = 0.10 at 490 K	[159]
2	M. Ito and T. Matsuda	$SrTiO_3$	HP @ 1400 °C, 2 h	25 MPa (Argon)	95.8%	ZT~0.092 at 870 K	[161]
		10 at.% Y-doped $SrTiO_3$			97.2%	ZT = 0.146 at 870 K	
3	Y. Wang et al.	5 at.% Gd-doped $SrO(SrTiO_3)_2$	HP @ 1450 °C, 1 h	36 MPa (Argon)	96–99%	ZT~0.24 at 1000 K	[162]
		5 at.% Nb-doped $SrO(SrTiO_3)_2$				ZT = 0.14 at 1000 K	
4	A. Kikuchi et al.	8 at.% La-doped $SrTiO_3$	SPS @ 1300 °C, 5 min	34 MPa (Vacuum)	97.7%	ZT = 0.37 at 1045 K	[158]
5	P.-P. Shang et al.	8 at.% La-doped $SrTiO_3$	SPS @ 1200 °C, 5 min	40 MPa (Vacuum)	91.6%	ZT = 0.08 at 679 K	[163]
6	N. Okinaka et al.	8 at.% La-doped $SrTiO_3$	SPS @ 1300 °C, 30 min	34 MPa (Vacuum)	>95%	ZT = 0.22 at 800 K	[164]

This effect is the main difference from the hot-pressing technology, which conducts the Joule heat to the material from the outside (from inductive or resistive heater). That results in a temperature gradient (temperature spatial non-uniformity) between the center and the periphery (surface) of ceramics, particularly at large sizes of green bodies, that may yield in non-uniform material in terms of chemical (phase) composition and microstructure. Additionally, hot pressing cycle takes a long time, because pressure can be applied only after holding for some time, which is necessary for temperature balancing along the sample. That is why we give the priority to the SPS method here.

Recently, D.Yu. Kosyanov et al. suggested a modified approach to fabrication of highly-dense fine-grained ceramics based on reactive SPS of nanopowders in the oxide systems with controlled particle size distribution, using Nd^{3+}:YAG as an example [165]. This route allows implementing external pressure, particle surface curvature (nanopowders of different sizes) and chemical reactions (phase transformations according to the scheme "starting oxides → intermediate phases → final product") simultaneously as driving forces of sintering to obtain uniform highly dense microstructure. Crystal lattice rearrangement during phase transitions activates diffusion-dislocation processes promoting effective densification of ceramics due to grain rotation and migration as a whole [166,167]. This allows the reduction of sintering time by 10–20 times as compared to non-reactive SPS of similar materials.

Given the abovementioned, the formation of biphase composite fine-grained TiO_2–$SrTiO_3$ ceramics should to be carried out via reactive SPS of strontium oxide SrO (formed by the decomposition of $SrCO_3$) and titania TiO_2. Checkered structure of ceramics will be provided by TiO_2 and $SrTiO_3$ phases taken in the ratio 50:50 vol.% that corresponds to the molar ratio of 73.835 mol.%:26.165 mol.%. Uniform distribution of the two phases will provide long-range mass transport between interface boundaries, which has a limiting effect of the atomic movement (excessive grain growth) [161]. Fabrication of highly-dense biphase ceramics with uniform distribution of two phases was demonstrated for Al_2O_3–$Y_3Al_5O_{12}$, Y_2O_3–MgO system [168–170].

$SrTiO_3$ formation proceeds in at least three stages, which was reported in detail here [171]. Phase and closed-type porosity formation is preceded by the sample's heating, which embraces the

decomposition of strontium carbonate $SrCO_3$ to strontium oxide SrO. Mass transfer in the depth of the product for the $SrO–TiO_2$ system is limited by titanium cations, which is in agreement with Sr–O and Ti–O bond strengths in $SrTiO_3$: Ti^{4+} ions are two times smaller than Sr^{2+} ones ($r(Ti^{4+})$ = 0.605 Å (6); $r(Sr^{2+})$ = 1.26 Å (8)).

Because reaction rate constant is inversely proportional to the radius of particles coated with agent (TiO_2 in our case) during sintering, particle size of the starting powder will play a major role in the kinetics of $SrTiO_3$ phase formation and densification. Niwa et al. reported a high-temperature gravimetric study on the kinetics of formation of $SrTiO_3$ [172]. The reactivity of starting materials and the kinetics of the reaction of strontium carbonate with titanium dioxide have been studied. The reaction of strontium carbonate $SrCO_3$ with rutile TiO_2 obeyed the nuclei growth rate equation, with an activation energy of 409 kJ·mol^{-1}. The kinetics of the reaction between strontium carbonate $SrCO_3$ and anatase TiO_2 was described by a diffusion-controlled rate equation with a much lower activation energy of 279 kJ·mol^{-1}. The difference between rutile and anatase in reacting with strontium carbonate has been related to the closer unit cell parameters of anatase and $SrTiO_3$ [173]. Thus, it is anatase TiO_2 nanopowders that are important to use for increasing the point of contact between starting materials and decreasing the activation energy to improve the reaction rate.

It is suggested that two-stage sintering (TSS) within reactive SPS to suppress the grain growth should be implemented. For example, in [174], non-reactive SPS was performed stepwise, i.e., the sample was primarily heated to 1220 °C and then immediately cooled down to 1000 °C followed by dwelling for 15 min without external pressure. As compared to ordinary "single-step" SPS (SSS) at 1250 °C for 30 min, authors obtained ceramic with nearly the same density of ~95% from theoretical. But for $SrTiO_3$, grains in samples sintered by TSS were some 40% smaller than in the samples sintered by the SSS method (0.35 μm vs. 0.56 μm). This effect is clearly illustrated by the scheme in Figure 13 [175]. The authors claimed in [174] that even larger differences in grain sizes obtained by TSS and SSS might be expected at higher final densities than 95%TD, when a uniaxial pressure is additionally used.
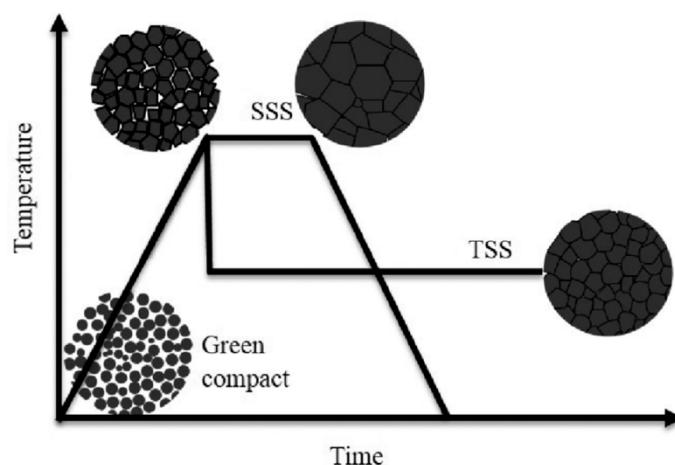

Figure 13. Schematic of densification of ceramics with grain growth during conventional single-step sintering (SSS) and densification without grain growth at lower second-step temperature during TSS with higher first-step temperature. © 2017 Sutharsini U, Thanihaichelvan M, Singh R. Published in Ref. [175] under CC BY 3.0 license. Available from: https://doi.org/10.5772/68083.

It is noteworthy that sintering in vacuum will initiate the formation of oxygen vacancies $V_O{''}$ due to extraction of O^{2-} ions from TiO_2 and $SrTiO_3$ structures. At the same time, concentrating limited electron-carriers occur most likely on $TiO_2/SrTiO_3$ interfaces as in the most loose, defect regions of TiO_2 and $SrTiO_3$ crystallites. On the other hand, the results of [176] indicate that intrinsic point defects in the pure $SrTiO_3$ ceramics are mainly $V_{Ti}{''''}$. Probably, $V_O{''}$ will be associated with a cation vacancy forming ($V_{Ti}{''''}$ + $2V_O{''}$) complex, namely, the Shottky defect. Federicci et al. in [177] reported a superionic conductor with a colossal dielectric constant for $Rb_2Ti_2O_5$ materials annealed under an

oxygen-depleted atmosphere (such as He, N_2, vacuum). They found that oxygen vacancies are created in the material, and the dielectric constant reaches the unprecedented value of 10^9. They proposed a possible mechanism of a Frenkel anionic defect. Additionally, they pointed out that another reason for such a high dielectric constant is that at least two ionic species of opposite signs are involved in the process. It was reported in the previous sections that oxygen vacancies are equivalent to n-doping to some extent [99], which is very important for 2DEG formation of heterointerfaces [27]. In other words, the formation of point defects in the TiO_2/$SrTiO_3$ structure will serve as additional factor enhancing the *ZT* value.

6. Summary and Future Prospect

Analysis of theoretical and experimental works has shown that multiple boundaries improves thermoelectric properties of the material because of two reasons, namely: Phonon filtration to drag only electrons (important for low temperatures) or simply intense phonon dissipation; 2DEG formation on the boundaries that filters electrons with respect to energy and possesses high thermoelectric characteristics itself. Structures able to generate 2DEG are produced by the only means of laser epitaxy that are hardly suitable for large scale manufacturing. Theoretical modelling of electronic structure suggests considering honeycomb architecture, which utilizes 2DEG features, yielding a drastic increase of the material's thermoelectric properties. But such architecture implies the special formation of thin films of the phase localizing 2DEG, which is a challenging and unresolved task. However, it is not necessary to build a 2D phase to localize 2DEG, because it can be formed on the interface between two oxide phases. This fact was not paid attention to in previous works related to materials with 2DEG.

That is why this review suggests to implement biphase ceramics based on $SrTiO_3$ and TiO_2. Its main feature is that 2DEG occurs spontaneously on the TiO_2/$SrTiO_3$ heterointerface, unlike ordinary 2DEG formation on specially formed thin film, because the conduction band edge of $SrTiO_3$ is 0.40 and 0.20 eV higher than that for anatase and rutile TiO_2, respectively. According to quantum chemical modelling of TiO_2(anatase)/$SrTiO_3$ and TiO_2(rutile)/$SrTiO_3$, chemical bonds were shown to appear on the interface for both crystal modifications. That is why the checkered order of TiO_2 and $SrTiO_3$ grains in the material's bulk will probably provide the single connected 2D surface along grain boundaries with 2DEG. Additionally, application of the SCC-DFTB method for modelling molecular structure of TiO_2 and $SrTiO_3$ interacting nanoparticles will enable us to predict optimal grain size and type/quantity of alloying agents for thermoelectrics with maximal *ZT* value.

The promising method of reactive SPS of anatase TiO_2 and SrO ($SrCO_3$) nanopowders is suggested for the preparation of highly dense material preserving the small (nanoscale) grain size of TiO_2, $SrTiO_3$ and thin interface layer between them. Uniform distribution of the two phases will provide long-range mass transport between interface boundaries, which has a limiting effect of the atomic movement (excessive grain growth). Fabrication of TiO_2−$SrTiO_3$ biphase nanoceramics will demonstrate that rapid sintering under pressure of two-phase oxide ceramics is the key towards the development of thermoelectric materials, utilizing 2DEG properties, for high-temperature applications.

Author Contributions: A.Z, D.K. conceived and drafted the work; A.Z, S.T. and D.K. designed the article, analyzed, and interpreted the reports present in literature; D.K. critically revised the manuscript.

References

1. Ohta, H. Thermoelectrics based on metal oxide thin films. In *Metal Oxide-Based Thin Film Structures*; Elsevier: Amsterdam, The Netherlands, 2018; pp. 441–464.
2. Jouhara, H.; Khordehgah, N.; Almahmoud, S.; Delpech, B.; Chauhan, A.; Tassou, S.A. Waste heat recovery technologies and applications. *Therm. Sci. Eng. Prog.* **2018**, *6*, 268–289. [CrossRef]

3. Rowe, D. (Ed.) *CRC Handbook of Thermoelectrics*; CRC Press: New York, NY, USA, 1995; ISBN 978-0-8493-0146-9.

4. Goldsmid, H.J. *Introduction to Thermoelectricity*; Springer Series in Materials Science; Springer: Berlin, Heidelberg, 2010; Volume 121, ISBN 978-3-642-00715-6.

5. Raj, B.; Van de Voorde, M.; Mahajan, Y. (Eds.) *Nanotechnology for Energy Sustainability*; Wiley-VCH Verlag GmbH & Co. KGaA: Weinheim, Germany, 2017; ISBN 9783527696109.

6. Abdul Khalid, K.A.; Leong, T.J.; Mohamed, K. Review on thermionic energy converters. *IEEE Trans. Electron Devices* **2016**, *63*, 2231–2241. [CrossRef]

7. Seebeck, T.J. *Magnetische Polarisation Der Metalle Und Erze Durch Temperatur-Differenz*; Abhandlungen der Königlichen Akademie der Wissenschaften: Berlin, Germany, 1823.

8. Peltier, J.C.A. Nouvelles expériences sur la caloricité des courants électrique. *Ann. Chim. Phys.* **1834**, *56*, 371–386.

9. Yin, Y.; Tudu, B.; Tiwari, A. Recent advances in oxide thermoelectric materials and modules. *Vacuum* **2017**, *146*, 356–374. [CrossRef]

10. Koumoto, K.; Wang, Y.; Zhang, R.; Kosuga, A.; Funahashi, R. Oxide thermoelectric materials: A nanostructuring approach. *Ann. Rev. Mater. Res.* **2010**, *40*, 363–394. [CrossRef]

11. Koumoto, K.; Funahashi, R.; Guilmeau, E.; Miyazaki, Y.; Weidenkaff, A.; Wang, Y.; Wan, C. Thermoelectric ceramics for energy harvesting. *J. Am. Ceram. Soc.* **2013**, *96*, 1–23. [CrossRef]

12. Ioffe, A.F.; Stil'bans, L.S.; Iordanishvili, E.K.; Stavitskaya, T.S.; Gelbtuch, A.; Vineyard, G. Semiconductor thermoelements and thermoelectric cooling. *Phys. Today* **1959**, *12*, 42. [CrossRef]

13. Tritt, T.M.; Subramanian, M.A. Thermoelectric materials, phenomena, and applications: A bird's eye view. *MRS Bull.* **2006**, *31*, 188–198. [CrossRef]

14. Snyder, G.J.; Toberer, E.S. Complex thermoelectric materials. *Nat. Mater.* **2008**, *7*, 105–114. [CrossRef]

15. Venkatasubramanian, R.; Siivola, E.; Colpitts, T.; O'Quinn, B. Thin-film thermoelectric devices with high room-temperature figures of merit. *Nature* **2001**, *413*, 597–602. [CrossRef]

16. Zhao, L.-D.; Lo, S.-H.; Zhang, Y.; Sun, H.; Tan, G.; Uher, C.; Wolverton, C.; Dravid, V.P.; Kanatzidis, M.G. Ultralow thermal conductivity and high thermoelectric figure of merit in SnSe crystals. *Nature* **2014**, *508*, 373–377. [CrossRef] [PubMed]

17. Rhyee, J.-S; Lee, K.H.; Lee, S.M.; Cho, E.; Kim, S.I.; Lee, E.; Kwon, Y.S.; Shim, J.H.; Kotliar, G. Peierls distortion as a route to high thermoelectric performance in In$_4$Se$_{3-\delta}$ crystals. *Nature* **2009**, *459*, 965–968. [CrossRef] [PubMed]

18. Snyder, G.J.; Christensen, M.; Nishibori, E.; Caillat, T.; Iversen, B.B. Disordered zinc in Zn$_4$Sb$_3$ with phonon-glass and electron-crystal thermoelectric properties. *Nat. Mater.* **2004**, *3*, 458–463. [CrossRef] [PubMed]

19. Matsuno, J.; Ogawa, N.; Yasuda, K.; Kagawa, F.; Koshibae, W.; Nagaosa, N.; Tokura, Y.; Kawasaki, M. Interface-driven topological Hall effect in SrRuO$_3$-SrIrO$_3$ bilayer. *Sci. Adv.* **2016**, *2*, e1600304. [CrossRef] [PubMed]

20. Zhao, L.-D.; Tan, G.; Hao, S.; He, J.; Pei, Y.; Chi, H.; Wang, H.; Gong, S.; Xu, H.; Dravid, V.P.; et al. Ultrahigh power factor and thermoelectric performance in hole-doped single-crystal SnSe. *Science* **2016**, *351*, 141–144. [CrossRef]

21. Hsu, K.F.; Loo, S.; Guo, F.; Chen, W.; Dyck, J.S.; Uher, C.; Hogan, T.; Polychroniadis, E.K.; Kanatzidis, M.G. Cubic AgPb$_m$SbTe$_{2+m}$: Bulk thermoelectric materials with high figure of merit. *Science* **2004**, *303*, 818–821. [CrossRef] [PubMed]

22. Chung, D.-Y.; Hogan, T.; Brazis, P.; Rossi-Lane, M.; Kannewurf, C.; Bastea, M.; Uher, C.; Kanatzidis, M.G. CsBi$_4$Te$_6$: A high-performance thermoelectric material for low-temperature applications. *Science* **2000**, *287*, 1024–1027. [CrossRef]

23. Kim, S.I.; Lee, K.H.; Mun, H.A.; Kim, H.S.; Hwang, S.W.; Roh, J.W.; Yang, D.J.; Shin, W.H.; Li, X.S.; Lee, Y.H.; et al. Dense dislocation arrays embedded in grain boundaries for high-performance bulk thermoelectrics. *Science* **2015**, *348*, 109–114. [CrossRef]

24. Romanjek, K.; Vesin, S.; Aixala, L.; Baffie, T.; Bernard-Granger, G.; Dufourcq, J. High-Performance Silicon–Germanium-Based Thermoelectric Modules for Gas Exhaust Energy Scavenging. *J. Electron. Mater.* **2015**, *44*, 2192–2202. [CrossRef]

25. Koumoto, K.; Terasaki, I.; Funahashi, R. Complex oxide materials for potential thermoelectric applications. *MRS Bull.* **2006**, *31*, 206–210. [CrossRef]

26. Szczech, J.R.; Higgins, J.M.; Jin, S. Enhancement of the thermoelectric properties in nanoscale and nanostructured materials. *J. Mater. Chem.* **2011**, *21*, 4037–4055. [CrossRef]

27. Ohta, H.; Kim, S.; Mune, Y.; Mizoguchi, T.; Nomura, K.; Ohta, S.; Nomura, T.; Nakanishi, Y.; Ikuhara, Y.; Hirano, M.; et al. Giant thermoelectric Seebeck coefficient of a two-dimensional electron gas in $SrTiO_3$. *Nat. Mater.* **2007**, *6*, 129–134. [CrossRef] [PubMed]

28. Hogarth, C.A.; Andrews, J.P. XXV. Variation with oxygen pressure of the thermoelectric power of cadmium oxide. *London Edinburgh Dublin Philos. Mag. J. Sci.* **1949**, *40*, 273–282. [CrossRef]

29. Parravano, G. Thermoelectric behavior of nickel oxide. *J. Chem. Phys.* **1955**, *23*, 5–10. [CrossRef]

30. Hutson, A.R. Electronic properties of ZnO. *J. Phys. Chem. Solids* **1959**, *8*, 467–472. [CrossRef]

31. Arvin, M.J. Electrical conductivity and thermoelectric power of indium oxide. *J. Phys. Chem. Solids* **1962**, *23*, 1681–1683. [CrossRef]

32. Frederikse, H.P.R.; Thurber, W.R.; Hosler, W.R. Electronic transport in strontium titanate. *Phys. Rev.* **1964**, *134*, A442–A445. [CrossRef]

33. Thurber, W.R.; Mante, A.J.H. Thermal conductivity and thermoelectric power of rutile (TiO_2). *Phys. Rev.* **1965**, *139*, A1655–A1665. [CrossRef]

34. Marley, J.A.; Dockerty, R.C. Electrical properties of stannic oxide single crystals. *Phys. Rev.* **1965**, *140*, A304–A310. [CrossRef]

35. Young, A.P.; Schwartz, C.M. Electrical conductivity and thermoelectric power of Cu_2O. *J. Phys. Chem. Solids* **1969**, *30*, 249–252. [CrossRef]

36. Bednorz, J.G.; Müller, K.A. Possible high T_c superconductivity in the Ba-La-Cu-O system. *Zeitschrift Phys. B Condens. Matter* **1986**, *64*, 189–193. [CrossRef]

37. Wu, M.K.; Ashburn, J.R.; Torng, C.J.; Hor, P.H.; Meng, R.L.; Gao, L.; Huang, Z.J.; Wang, Y.Q.; Chu, C.W. Superconductivity at 93 K in a new mixed-phase Y-Ba-Cu-O compound system at ambient pressure. *Phys. Rev. Lett.* **1987**, *58*, 908–910. [CrossRef] [PubMed]

38. Cooper, J.R.; Alavi, B.; Zhou, L.-W.; Beyermann, W.P.; Grüner, G. Thermoelectric power of some high-T_c oxides. *Phys. Rev. B* **1987**, *35*, 8794–8796. [CrossRef] [PubMed]

39. Chen, J.T.; McEwan, C.J.; Wenger, L.E.; Logothetis, E.M. Determination of charge carriers in superconducting La-Ba-Cu-O by thermoelectric measurements. *Phys. Rev. B* **1987**, *35*, 7124–7125. [CrossRef] [PubMed]

40. Lee, S.; Lee, J.; Suh, B.; Moon, S.; Lim, C.; Khim, Z. Thermoelectric power and superconducting properties of $Y_1Ba_2Cu_3O_{7-\delta}$ and $R_1Ba_2Cu_3O_{7-\delta}$. *Phys. Rev. B* **1988**, *37*, 2285–2288. [CrossRef] [PubMed]

41. Mitra, N.; Trefny, J.; Yarar, B.; Pine, G.; Sheng, Z.Z.; Hermann, A.M. Thermoelectric power of the Tl-Ca-Ba-Cu-O superconductor. *Phys. Rev. B* **1988**, *38*, 7064–7066. [CrossRef] [PubMed]

42. Ohtaki, M.; Koga, H.; Tokunaga, T.; Eguchi, K.; Arai, H. Electrical transport properties and high-temperature thermoelectric performance of $(Ca_{0.9}M_{0.1})MnO_3$ (M=Y, La, Ce, Sm, In, Sn, Sb, Pb, Bi). *J. Solid State Chem.* **1995**, *120*, 105–111. [CrossRef]

43. Ohtaki, M.; Tsubota, T.; Eguchi, K.; Arai, H. High-temperature thermoelectric properties of $(Zn_{1-x}Al_x)O$. *J. Appl. Phys.* **1996**, *79*, 1816–1818. [CrossRef]

44. Terasaki, I.; Sasago, Y.; Uchinokura, K. Large thermoelectric power in $NaCo_2O_4$ single crystals. *Phys. Rev. B* **1997**, *56*, R12685–R12687. [CrossRef]

45. Masset, A.C.; Michel, C.; Maignan, A.; Hervieu, M.; Toulemonde, O.; Studer, F.; Raveau, B.; Hejtmanek, J. Misfit-layered cobaltite with an anisotropic giant magnetoresistance: $Ca_3Co_4O_9$. *Phys. Rev. B* **2000**, *62*, 166–175. [CrossRef]

46. Funahashi, R.; Matsubara, I.; Ikuta, H.; Takeuchi, T.; Mizutani, U.; Sodeoka, S. An oxide single crystal with high thermoelectric performance in air. *J. Appl. Phys. Jpn.* **2000**, *39*, 1127. [CrossRef]

47. Okuda, T.; Nakanishi, K.; Miyasaka, S.; Tokura, Y. Large thermoelectric response of metallic perovskites: $Sr_{1-x}La_xTiO_3$ (0 <~ x <~ 0.1). *Phys. Rev. B* **2001**, *63*, 113104. [CrossRef]

48. Ohta, S.; Nomura, T.; Ohta, H.; Koumoto, K. High-temperature carrier transport and thermoelectric properties of heavily La- or Nb-doped $SrTiO_3$ single crystals. *J. Appl. Phys.* **2005**, *97*, 034106. [CrossRef]

49. Ohta, S.; Nomura, T.; Ohta, H.; Hirano, M.; Hosono, H.; Koumoto, K. Large thermoelectric performance of heavily Nb-doped $SrTiO_3$ epitaxial film at high temperature. *Appl. Phys. Lett.* **2005**, *87*, 092108. [CrossRef]

50. Fergus, J.W. Oxide materials for high temperature thermoelectric energy conversion. *J. Eur. Ceram. Soc.* **2012**, *32*, 525–540. [CrossRef]

51. Tritt, T.M. Thermoelectric Materials: Principles, Structure, Properties, and Applications. In *Encyclopedia of Materials: Science and Technology*; Elsevier: Amsterdam, The Netherlands, 2002; pp. 1–11.

52. Walia, S.; Balendhran, S.; Nili, H.; Zhuiykov, S.; Rosengarten, G.; Wang, Q.H.; Bhaskaran, M.; Sriram, S.; Strano, M.S.; Kalantar-zadeh, K. Transition metal oxides—Thermoelectric properties. *Prog. Mater. Sci.* **2013**, *58*, 1443–1489. [CrossRef]

53. Keyes, R.W. High-Temperature thermal conductivity of insulating crystals: Relationship to the melting point. *Phys. Rev.* **1959**, *115*, 564–567. [CrossRef]

54. Vavilov, M.G.; Stone, A.D. Failure of the Wiedemann-Franz law in mesoscopic conductors. *Phys. Rev. B* **2005**, *72*, 205107. [CrossRef]

55. Chen, Z.-G.; Han, G.; Yang, L.; Cheng, L.; Zou, J. Nanostructured thermoelectric materials: Current research and future challenge. *Prog. Nat. Sci. Mater. Int.* **2012**, *22*, 535–549. [CrossRef]

56. Tritt, T.M. Thermoelectric phenomena, materials, and applications. *Annu. Rev. Mater. Res.* **2011**, *41*, 433–448. [CrossRef]

57. Muta, H.; Kurosaki, K.; Yamanaka, S. Thermoelectric properties of rare earth doped $SrTiO_3$. *J. Alloys Compd.* **2003**, *350*, 292–295. [CrossRef]

58. Muta, H.; Kurosaki, K.; Yamanaka, S. Thermoelectric properties of doped $BaTiO_3$–$SrTiO_3$ solid solution. *J. Alloys Compd.* **2004**, *368*, 22–24. [CrossRef]

59. Yamamoto, M.; Ohta, H.; Koumoto, K. Thermoelectric phase diagram in a $CaTiO_3$–$SrTiO_3$–$BaTiO_3$ system. *Appl. Phys. Lett.* **2007**, *90*, 072101. [CrossRef]

60. Kato, K.; Yamamoto, M.; Ohta, S.; Muta, H.; Kurosaki, K.; Yamanaka, S.; Iwasaki, H.; Ohta, H.; Koumoto, K. The effect of Eu substitution on thermoelectric properties of $SrTi_{0.8}Nb_{0.2}O_3$. *J. Appl. Phys.* **2007**, *102*, 116107. [CrossRef]

61. Liu, J.; Wang, C.L.; Li, Y.; Su, W.B.; Zhu, Y.H.; Li, J.C.; Mei, L.M. Influence of rare earth doping on thermoelectric properties of $SrTiO_3$ ceramics. *J. Appl. Phys.* **2013**, *114*, 223714. [CrossRef]

62. Kovalevsky, A.V.; Populoh, S.; Patrício, S.G.; Thiel, P.; Ferro, M.C.; Fagg, D.P.; Frade, J.R.; Weidenkaff, A. Design of $SrTiO_3$-based thermoelectrics by tungsten substitution. *J. Phys. Chem. C* **2015**, *119*, 4466–4478. [CrossRef]

63. Cui, Y.; He, J.; Amow, G.; Kleinke, H. Thermoelectric properties of n-type double substituted $SrTiO_3$ bulk materials. *Dalt. Trans.* **2010**, *39*, 1031–1035. [CrossRef]

64. Putri, Y.E.; Said, S.M.; Diantoro, M. Nanoarchitectured titanium complexes for thermal mitigation in thermoelectric materials. *Renew. Sustain. Energy Rev.* **2019**, *101*, 346–360. [CrossRef]

65. Zhou, J.; Liao, B.; Qiu, B.; Huberman, S.; Esfarjani, K.; Dresselhaus, M.S.; Chen, G. Ab initio optimization of phonon drag effect for lower-temperature thermoelectric energy conversion. *Proc. Natl. Acad. Sci. USA* **2015**, *112*, 14777–14782. [CrossRef]

66. Cain, T.A.; Kajdos, A.P.; Stemmer, S. La-doped $SrTiO_3$ films with large cryogenic thermoelectric power factors. *Appl. Phys. Lett.* **2013**, *102*, 182101. [CrossRef]

67. Cutler, M.; Mott, N.F. Observation of anderson localization in an electron gas. *Phys. Rev.* **1969**, *181*, 1336–1340. [CrossRef]

68. Heremans, J.P. Low-dimensional thermoelectricity. *Acta Phys. Pol. A* **2005**, *108*, 609–634. [CrossRef]

69. Zhang, R.; Wang, C.; Li, J.; Koumoto, K. Simulation of thermoelectric performance of bulk $SrTiO_3$ with two-dimensional electron gas grain boundaries. *J. Am. Ceram. Soc.* **2010**, *93*, 1677–1681.

70. Ohtomo, A.; Hwang, H.Y. A high-mobility electron gas at the $LaAlO_3$/$SrTiO_3$ heterointerface. *Nature* **2004**, *427*, 423–426. [CrossRef] [PubMed]

71. Reyren, N.; Thiel, S.; Caviglia, A.D.; Kourkoutis, L.F.; Hammerl, G.; Richter, C.; Schneider, C.W.; Kopp, T.; Ruetschi, A.-S.; Jaccard, D.; et al. Superconducting interfaces between insulating oxides. *Science* **2007**, *317*, 1196–1199. [CrossRef]

72. Pallecchi, I.; Telesio, F.; Marré, D.; Li, D.; Gariglio, S.; Triscone, J.-M.; Filippetti, A. Large phonon-drag enhancement induced by narrow quantum confinement at the $LaAlO_3$/$SrTiO_3$ interface. *Phys. Rev. B* **2016**, *93*, 195309. [CrossRef]

73. Perna, P.; Maccariello, D.; Radovic, M.; Scotti di Uccio, U.; Pallecchi, I.; Codda, M.; Marré, D.; Cantoni, C.; Gazquez, J.; Varela, M.; et al. Conducting interfaces between band insulating oxides: The $LaGaO_3$/$SrTiO_3$ heterostructure. *Appl. Phys. Lett.* **2010**, *97*, 152111. [CrossRef]

74. Stemmer, S.; James, A.S. Two-dimensional electron gases at complex oxide interfaces. *Ann. Rev. Mater. Res.* **2014**, *44*, 151–171. [CrossRef]

75. Cain, T.A.; Moetakef, P.; Jackson, C.A.; Stemmer, S. Modulation doping to control the high-density electron gas at a polar/non-polar oxide interface. *Appl. Phys. Lett.* **2012**, *101*, 111604. [CrossRef]

76. Moetakef, P.; Cain, T.A.; Ouellette, D.G.; Zhang, J.Y.; Klenov, D.O.; Janotti, A.; Van de Walle, C.G.; Rajan, S.; Allen, S.J.; Stemmer, S. Electrostatic carrier doping of $GdTiO_3/SrTiO_3$ interfaces. *Appl. Phys. Lett.* **2011**, *99*, 232116. [CrossRef]

77. Moetakef, P.; Jackson, C.A.; Hwang, J.; Balents, L.; Allen, S.J.; Stemmer, S. Toward an artificial Mott insulator: Correlations in confined high-density electron liquids in $SrTiO_3$. *Phys. Rev. B* **2012**, *86*, 201102. [CrossRef]

78. Cain, T.A.; Lee, S.; Moetakef, P.; Balents, L.; Stemmer, S.; James, A.S. Seebeck coefficient of a quantum confined, high-electron-density electron gas in $SrTiO_3$. *Appl. Phys. Lett.* **2012**, *100*, 161601. [CrossRef]

79. Kim, J.S.; Seo, S.S.A.; Chisholm, M.F.; Kremer, R.K.; Habermeier, H.-U.; Keimer, B.; Lee, H.N. Nonlinear Hall effect and multichannel conduction in $LaTiO_3/SrTiO_3$ superlattices. *Phys. Rev. B* **2010**, *82*, 201407. [CrossRef]

80. Tsukazaki, A.; Ohtomo, A.; Kita, T.; Ohno, Y.; Ohno, H.; Kawasaki, M. Quantum Hall effect in polar oxide heterostructures. *Science* **2007**, *315*, 1388–1391. [CrossRef] [PubMed]

81. Tsukazaki, A.; Akasaka, S.; Nakahara, K.; Ohno, Y.; Ohno, H.; Maryenko, D.; Ohtomo, A.; Kawasaki, M. Observation of the fractional quantum Hall effect in an oxide. *Nat. Mater.* **2010**, *9*, 889–893. [CrossRef]

82. Schlom, D.G.; Pfeiffer, L.N. Upward mobility rocks! *Nat. Mater.* **2010**, *9*, 881–883. [CrossRef] [PubMed]

83. Kozuka, Y.; Tsukazaki, A.; Maryenko, D.; Falson, J.; Akasaka, S.; Nakahara, K.; Nakamura, S.; Awaji, S.; Ueno, K.; Kawasaki, M. Insulating phase of a two-dimensional electron gas in $Mg_xZn_{1-x}O/ZnO$ heterostructures below $\nu = 1/3$. *Phys. Rev. B* **2011**, *84*, 033304. [CrossRef]

84. Dingle, R.; Störmer, H.L.; Gossard, A.C.; Wiegmann, W. Electron mobilities in modulation-doped semiconductor heterojunction superlattices. *Appl. Phys. Lett.* **1978**, *33*, 665–667. [CrossRef]

85. Eisenstein, J.P.; Cooper, K.B.; Pfeiffer, L.N.; West, K.W. Insulating and fractional quantum hall states in the first excited landau level. *Phys. Rev. Lett.* **2002**, *88*, 076801. [CrossRef]

86. Umansky, V.; Heiblum, M.; Levinson, Y.; Smet, J.; Nübler, J.; Dolev, M. MBE growth of ultra-low disorder 2DEG with mobility exceeding 35×10^6 cm^2/Vs. *J. Cryst. Growth* **2009**, *311*, 1658–1661. [CrossRef]

87. Mimura, T.; Hiyamizu, S.; Fujii, T.; Nanbu, K. A New field-effect transistor with selectively doped $GaAs/n-Al_xGa_{1-x}As$ heterojunctions. *Jpn. J. Appl. Phys.* **1980**, *19*, L225–L227. [CrossRef]

88. Delagebeaudeuf, D.; Linh, N.T. Metal-(n) AlGaAs-GaAs two-dimensional electron gas FET. *IEEE Trans. Electron Devices* **1982**, *29*, 955–960. [CrossRef]

89. Schafranek, R.; Baniecki, J.D.; Ishii, M.; Kotaka, Y.; Yamanka, K.; Kurihara, K. Band offsets at the epitaxial $SrTiO_3/SrZrO_3$ (001) heterojunction. *J. Phys. D. Appl. Phys.* **2012**, *45*, 055303. [CrossRef]

90. Janotti, A.; Bjaalie, L.; Gordon, L.; Van de Walle, C.G. Controlling the density of the two-dimensional electron gas at the $SrTiO_3/LaAlO_3$ interface. *Phys. Rev. B* **2012**, *86*, 241108. [CrossRef]

91. Berner, G.; Müller, A.; Pfaff, F.; Walde, J.; Richter, C.; Mannhart, J.; Thiess, S.; Gloskovskii, A.; Drube, W.; Sing, M.; et al. Band alignment in $LaAlO_3/SrTiO_3$ oxide heterostructures inferred from hard x-ray photoelectron spectroscopy. *Phys. Rev. B* **2013**, *88*, 115111. [CrossRef]

92. Chambers, S.A.; Engelhard, M.H.; Shutthanandan, V.; Zhu, Z.; Droubay, T.C.; Qiao, L.; Sushko, P.V.; Feng, T.; Lee, H.D.; Gustafsson, T.; et al. Instability, intermixing and electronic structure at the epitaxial $LaAlO_3/SrTiO_3$ (001) heterojunction. *Surf. Sci. Rep.* **2010**, *65*, 317–352. [CrossRef]

93. Lim, S.-G.; Kriventsov, S.; Jackson, T.N.; Haeni, J.H.; Schlom, D.G.; Balbashov, A.M.; Uecker, R.; Reiche, P.; Freeouf, J.L.; Lucovsky, G. Dielectric functions and optical bandgaps of high-K dielectrics for metal-oxide-semiconductor field-effect transistors by far ultraviolet spectroscopic ellipsometry. *J. Appl. Phys.* **2002**, *91*, 4500–4505. [CrossRef]

94. Lee, Y.S.; Lee, J.S.; Noh, T.W.; Byun, D.Y.; Yoo, K.S.; Yamaura, K.; Takayama-Muromachi, E. Systematic trends in the electronic structure parameters of the 4d transition-metal oxides $SrMO_3$ (M=Zr, Mo, Ru, and Rh). *Phys. Rev. B* **2003**, *67*, 113101. [CrossRef]

95. Qiao, L.; Droubay, T.C.; Kaspar, T.C.; Sushko, P.V.; Chambers, S.A. Cation mixing, band offsets and electric fields at $LaAlO_3/SrTiO_3$ (001) heterojunctions with variable La:Al atom ratio. *Surf. Sci.* **2011**, *605*, 1381–1387. [CrossRef]

96. Delugas, P.; Filippetti, A.; Gadaleta, A.; Pallecchi, I.; Marré, D.; Fiorentini, V. Large band offset as driving force of two-dimensional electron confinement: The case of $SrTiO_3/SrZrO_3$ interface. *Phys. Rev. B* **2013**, *88*, 115304. [CrossRef]

97. Kajdos, A.P.; Ouellette, D.G.; Cain, T.A.; Stemmer, S. Two-dimensional electron gas in a modulation-doped SrTiO$_3$/Sr(Ti,Zr)O$_3$ heterostructure. *Appl. Phys. Lett.* **2013**, *103*, 082120. [CrossRef]

98. Fujisawa, J.; Eda, T.; Hanaya, M. Comparative study of conduction-band and valence-band edges of TiO$_2$, SrTiO$_3$, and BaTiO$_3$ by ionization potential measurements. *Chem. Phys. Lett.* **2017**, *685*, 23–26. [CrossRef]

99. Shanthi, N.; Sarma, D.D. Electronic structure of electron doped SrTiO$_3$: SrTiO$_{3-\delta}$ and Sr$_{1-x}$La$_x$TiO$_3$. *Phys. Rev. B* **1998**, *57*, 2153–2158. [CrossRef]

100. Abutaha, A.I.; Kumar, S.R.S.; Li, K.; Dehkordi, A.M.; Tritt, T.M.; Alshareef, H.N. Enhanced thermoelectric figure-of-merit in thermally robust, nanostructured superlattices based on SrTiO$_3$. *Chem. Mater.* **2015**, *27*, 2165–2171. [CrossRef]

101. Mune, Y.; Ohta, H.; Koumoto, K.; Mizoguchi, T.; Ikuhara, Y. Enhanced Seebeck coefficient of quantum-confined electrons in SrTiO$_3$/SrTi$_{0.8}$Nb$_{0.2}$O$_3$ superlattices. *Appl. Phys. Lett.* **2007**, *91*, 192105. [CrossRef]

102. Ohta, H.; Mune, Y.; Koumoto, K.; Mizoguchi, T.; Ikuhara, Y. Critical thickness for giant thermoelectric Seebeck coefficient of 2DEG confined in SrTiO$_3$/SrTi$_{0.8}$Nb$_{0.2}$O$_3$ superlattices. *Thin Solid Films* **2008**, *516*, 5916–5920. [CrossRef]

103. Park, N.-H.; Dang, F.; Wan, C.; Seo, W.-S.; Koumoto, K. Self-originating two-step synthesis of core–shell structured La-doped SrTiO$_3$ nanocubes. *J. Asian Ceram. Soc.* **2013**, *1*, 35–40. [CrossRef]

104. Park, N.-H.; Akamatsu, T.; Itoh, T.; Izu, N.; Shin, W. Rapid synthesis and formation mechanism of core-shell-structured La-doped SrTiO$_3$ with a Nb-doped shell. *Materials* **2015**, *8*, 3992–4003. [CrossRef]

105. Wang, Y.; Zhang, X.; Shen, L.; Bao, N.; Wan, C.; Park, N.-H.; Koumoto, K.; Gupta, A. Nb-doped grain boundary induced thermoelectric power factor enhancement in La-doped SrTiO$_3$ nanoceramics. *J. Power Sources* **2013**, *241*, 255–258. [CrossRef]

106. Hays, C.C.; Zhou, J.-S.; Markert, J.T.; Goodenough, J.B. Electronic transition in La$_{1-x}$Sr$_x$TiO$_3$. *Phys. Rev. B* **1999**, *60*, 10367–10373. [CrossRef]

107. Kear, B.H.; Al-Sharab, J.F.; Sadangi, R.K.; Deutsch, S.; Kavukcuoglu, N.B.; Tse, S.D.; Mann, A.; Voronov, O.A.; Nordahl, C.S. On the conversion of bulk polycrystalline Y$_2$O$_3$ into the nanocrystalline state. *J. Am. Ceram. Soc.* **2011**, *94*, 1744–1746. [CrossRef]

108. Guinea, F.; Horovitz, B.; Le Doussal, P. Gauge field induced by ripples in graphene. *Phys. Rev. B* **2008**, *77*, 205421. [CrossRef]

109. Zubkov, M.A.; Volovik, G.E. Emergent gravity in graphene. *J. Phys. Conf. Ser.* **2015**, *607*, 012020. [CrossRef]

110. Li, E.; Wang, N.; He, H.; Chen, H. Improved thermoelectric performances of SrTiO$_3$ ceramic doped with Nb by surface modification of nanosized titania. *Nanoscale Res. Lett.* **2016**, *11*, 188. [CrossRef] [PubMed]

111. Katagiri, K.; Ohno, K.; Masuda, Y.; Koumoto, K. Growth behavior of TiO$_2$ particles via the liquid phase deposition process. *J. Ceram. Soc. Jpn.* **2007**, *115*, 831–834. [CrossRef]

112. Klemens, P.G. Thermal conductivity of inhomogeneous materials. *Int. J. Thermophys.* **1989**, *10*, 1213–1219. [CrossRef]

113. El Khal, H.; Cordier, A.; Batis, N.; Siebert, E.; Georges, S.; Steil, M.C. Effect of porosity on the electrical conductivity of LAMOX materials. *Solid State Ionics* **2017**, *304*, 75–84. [CrossRef]

114. Maxwell, J.C. *A Treatise on Electricity and Magnetism*; Cambridge University Press: Cambridge, UK, 2010; ISBN 9780511709333.

115. Bird, R.B.; Stewart, W.E.; Lightfoot, E.N. Transport phenomena. *AIChE J.* **1961**, *7*, 5J–6J.

116. Bergman, D.J. The dielectric constant of a composite material—A problem in classical physics. *Phys. Rep.* **1978**, *43*, 377–407. [CrossRef]

117. Bergman, D.J. Rigorous bounds for the complex dielectric constant of a two-component composite. *Ann. Phys.* **1982**, *138*, 78–114. [CrossRef]

118. Carman, P.C. *Flow of Gases through Porous Media*; Academic Press: New York, NY, USA, 1956.

119. Ha, T.-J.; Park, H.-H.; Jung, S.-Y.; Yoon, S.-J.; Kim, J.-S.; Jang, H.W. Effect of porosity on the Seebeck coefficient of mesoporous TiO$_2$ thin films. *Thin Solid Films* **2010**, *518*, 7196–7198. [CrossRef]

120. Lee, H.; Vashaee, D.; Wang, D.Z.; Dresselhaus, M.S.; Ren, Z.F.; Chen, G. Effects of nanoscale porosity on thermoelectric properties of SiGe. *J. Appl. Phys.* **2010**, *107*, 094308. [CrossRef]

121. Ohta, S.; Ohta, H.; Koumoto, K. Grain size dependence of thermoelectric performance of Nb-doped SrTiO$_3$ polycrystals. *J. Ceram. Soc. Jpn.* **2006**, *114*, 102–105. [CrossRef]

122. Navrotsky, A.; Kleppa, O.J. Enthalpy of the anatase-rutile transformation. *J. Am. Ceram. Soc.* **1967**, *50*, 626. [CrossRef]

123. Rubenis, K.; Ozoliņš, J.; Pūra, A.; Ločs, J.; Reimanis, M.; Narkevica, I.; Līga, B.-C. The influence of thermal treatment on the properties of TiO$_2$ ceramics obtained by extrusion. *Mater. Sci. Appl. Chem.* **2012**, *25*, 71–75.

124. Zhao, L.; Wang, J.; Gai, Z.; Li, J.; Liu, J.; Wang, J.; Wang, C.; Wang, X. Annealing effects on the structural and dielectric properties of (Nb + In) co-doped rutile TiO$_2$ ceramics. *RSC Adv.* **2019**, *9*, 8364–8368. [CrossRef]

125. D'Amico, N.R.; Cantele, G.; Ninno, D. First principles calculations of the band offset at SrTiO$_3$–TiO$_2$ interfaces. *Appl. Phys. Lett.* **2012**, *101*, 141606. [CrossRef]

126. Chambers, S.A.; Ohsawa, T.; Wang, C.M.; Lyubinetsky, I.; Jaffe, J.E. Band offsets at the epitaxial anatase TiO$_2$/n-SrTiO$_3$(001) interface. *Surf. Sci.* **2009**, *603*, 771–780. [CrossRef]

127. Hasnip, P.J.; Refson, K.; Probert, M.I.J.; Yates, J.R.; Clark, S.J.; Pickard, C.J. Density functional theory in the solid state. *Philos. Trans. A Math. Phys. Eng. Sci.* **2014**, *372*, 20130270. [CrossRef]

128. Pacchioni, G. First principles calculations on oxide-based heterogeneous catalysts and photocatalysts: Problems and advances. *Catal. Lett.* **2014**, *145*, 80–94. [CrossRef]

129. Kohn, W.; Sham, L.J. Self-consistent equations including exchange and correlation effects. *Phys. Rev.* **1965**, *140*, A1133–A1138. [CrossRef]

130. Blöchl, P.E. Projector augmented-wave method. *Phys. Rev. B* **1994**, *50*, 17953–17979. [CrossRef] [PubMed]

131. Kresse, G.; Joubert, D. From ultrasoft pseudopotentials to the projector augmented-wave method. *Phys. Rev. B* **1999**, *59*, 1758–1775. [CrossRef]

132. Vanderbilt, D. Soft self-consistent pseudopotentials in a generalized eigenvalue formalism. *Phys. Rev. B* **1990**, *41*, 7892–7895. [CrossRef]

133. Singh, D.J.; Nordstrom, L. *Planewaves, Pseudopotentials and the LAPW Method*, 2nd ed.; Springer: New York, NY, USA, 2006; pp. 1–134.

134. Anisimov, V.I.; Aryasetiawan, F.; Lichtenstein, A.I. First-principles calculations of the electronic structure and spectra of strongly correlated systems: The LDA+U method. *J. Phys. Condens. Matter* **1997**, *9*, 767–808. [CrossRef]

135. Hubbard, J. Electron correlations in narrow energy bands. *Proc. R. Soc. London, Ser. A* **1965**, *276*, 238–257.

136. Dudarev, S.L.; Botton, G.A.; Savrasov, S.Y.; Humphreys, C.J.; Sutton, A.P. Electron-energy-loss spectra and the structural stability of nickel oxide: An LSDA+U study. *Phys. Rev. B* **1998**, *57*, 1505–1509. [CrossRef]

137. Cococcioni, M. *The LDA+U Approach: A Simple Hubbard Correction for Correlated Ground States. Correlated Electrons: From Models to Materials Modeling and simulation*; Forschungszentrum: Julich, Germany, 2012; pp. 4–33. ISBN 978-3-89336-796-2.

138. Himmetoglu, B.; Floris, A.; De Gironcoli, S.; Cococcioni, M. Hubbard-corrected DFT energy functionals: The LDA+U description of correlated systems. *Int. J. Quantum Chem.* **2014**, *114*, 14–49. [CrossRef]

139. Liu, X.; Sohlberg, K. Theoretical calculations on layered perovskites: Implications for photocatalysis. *Complex Metals* **2014**, *1*, 103–121. [CrossRef]

140. Becke, A.D. Density-functional thermochemistry. III. The role of exact exchange. *J. Chem. Phys.* **1993**, *98*, 5648–5652. [CrossRef]

141. Stephens, P.J.; Devlin, F.J.; Chabalowski, C.F.; Frisch, M.J. Ab initio calculation of vibrational absorption and circular dichroism spectra using density functional force fields. *J. Phys. Chem.* **1994**, *98*, 11623–11627. [CrossRef]

142. Perdew, J.P.; Burke, K.; Ernzerhof, M. Rationale for mixing exact exchange with density functional approximations. *J. Chem. Phys.* **1996**, *105*, 9982–9985. [CrossRef]

143. Paier, J.; Marsman, M.; Kresse, G. Why does the B3LYP hybrid functional fail for metals? *J. Chem. Phys.* **2007**, *127*, 024103. [CrossRef] [PubMed]

144. Perdew, J.P.; Chevary, J.A.; Vosko, S.H.; Jackson, K.A.; Pederson, M.R.; Singh, D.J.; Fiolhais, C. Atoms, molecules, solids, and surfaces: Applications of the generalized gradient approximation for exchange and correlation. *Phys. Rev. B* **1992**, *46*, 6671–6687. [CrossRef] [PubMed]

145. Wang, Z.; Sun, R.; Chen, C.; Saito, M.; Tsukimoto, S.; Ikuhara, Y. Structural and electronic impact of SrTiO$_3$ substrate on TiO$_2$ thin films. *J. Mater. Sci.* **2012**, *47*, 5148–5157. [CrossRef]

146. Xu, Z.; Salvador, P.; Kitchin, J.R. First-principles investigation of the epitaxial stabilization of oxide polymorphs: TiO$_2$ on (Sr,Ba)TiO$_3$. *ACS Appl. Mater. Interfaces* **2017**, *9*, 4106–4118. [CrossRef] [PubMed]

147. Maheu, C.; Cardenas, L.; Puzenat, E.; Afanasiev, P.; Geantet, C. UPS and UV spectroscopies combined to position the energy levels of TiO$_2$ anatase and rutile nanopowders. *Phys. Chem. Chem. Phys.* **2018**, *20*, 25629–25637. [CrossRef] [PubMed]

148. Selli, D.; Fazio, G.; Di Valentin, C. Modelling realistic TiO$_2$ nanospheres: A benchmark study of SCC-DFTB against hybrid DFT. *J. Chem. Phys.* **2017**, *147*, 164701. [CrossRef]

149. Hedin, L. New method for calculating the one-particle green's function with application to the electron-gas problem. *Phys. Rev.* **1965**, *139*, A796–A823. [CrossRef]

150. Labat, F.; Baranek, P.; Domain, C.; Minot, C.; Adamo, C. Density functional theory analysis of the structural and electronic properties of TiO$_2$ rutile and anatase polytypes: performances of different exchange-correlation functionals. *J. Chem. Phys.* **2007**, *126*, 154703. [CrossRef]

151. Patrick, C.E.; Giustino, F. GW quasiparticle bandgaps of anatase TiO$_2$ starting from DFT + U. *J. Phys. Condens. Matter* **2012**, *24*, 202201. [CrossRef] [PubMed]

152. Fazio, G.; Ferrighi, L.; Di Valentin, C. Spherical versus faceted anatase TiO$_2$ nanoparticles: A model study of structural and electronic properties. *J. Phys. Chem. C* **2015**, *35*, 20735–20746. [CrossRef]

153. Chiodo, L.; García-Lastra, J.M.; Iacomino, A.; Ossicini, S.; Zhao, J.; Petek, H.; Rubio, A. Self-energy and excitonic effects in the electronic and optical properties of TiO$_2$ crystalline phases. *Phys. Rev. B* **2010**, *82*, 045207. [CrossRef]

154. Tang, H.; Lévy, F.; Berger, H.; Schmid, P.E. Urbach tail of anatase TiO$_2$. *Phys. Rev. B* **1995**, *52*, 7771–7774. [CrossRef] [PubMed]

155. Bi, F.; Markov, S.; Wang, R.; Kwok, Y.; Zhou, W.; Liu, L.; Zheng, X.; Chen, G.; Yam, C. Enhanced photovoltaic properties induced by ferroelectric domain structures in organometallic halide perovskites. *J. Phys. Chem. C* **2017**, *121*, 11151–11158. [CrossRef]

156. Luschtinetz, R.; Frenzel, J.; Milek, T.; Seifert, G. Adsorption of phosphonic acid at the TiO$_2$ anatase (101) and rutile (110) surfaces. *J. Phys. Chem. C* **2009**, *113*, 5730–5740. [CrossRef]

157. Fox, H.; Newman, K.E.; Schneider, W.F.; Corcelli, S.A. Bulk and surface properties of rutile TiO$_2$ from self-consistent-charge density functional tight binding. *J. Chem. Theory Comput.* **2010**, *6*, 499–507. [CrossRef] [PubMed]

158. Kikuchi, A.; Okinaka, N.; Akiyama, T. A large thermoelectric figure of merit of La-doped SrTiO$_3$ prepared by combustion synthesis with post-spark plasma sintering. *Scr. Mater.* **2010**, *63*, 407–410. [CrossRef]

159. Obara, H.; Yamamoto, A.; Lee, C.-H.; Kobayashi, K.; Matsumoto, A.; Funahashi, R. Thermoelectric properties of Y-doped polycrystalline SrTiO$_3$. *Jpn. J. Appl. Phys.* **2004**, *43*, L540–L542. [CrossRef]

160. Papynov, E.K.; Shichalin, O.O.; Mayorov, V.Y.; Modin, E.B.; Portnyagin, A.S.; Tkachenko, I.A.; Belov, A.A.; Gridasova, E.A.; Tananaev, I.G.; Avramenko, V.A. Spark Plasma Sintering as a high-tech approach in a new generation of synthesis of nanostructured functional ceramics. *Nanotechnol. Russ.* **2017**, *12*, 49–61. [CrossRef]

161. Ito, M.; Matsuda, T. Thermoelectric properties of non-doped and Y-doped SrTiO$_3$ polycrystals synthesized by polymerized complex process and hot pressing. *J. Alloys Compd.* **2009**, *477*, 473–477. [CrossRef]

162. Wang, Y.; Lee, K.H.; Ohta, H.; Koumoto, K. Thermoelectric properties of electron doped SrO(SrTiO$_3$)$_n$ (n = 1,2) ceramics. *J. Appl. Phys.* **2009**, *105*, 103701. [CrossRef]

163. Shang, P.-P.; Zhang, B.-P.; Li, J.-F.; Ma, N. Effect of sintering temperature on thermoelectric properties of La-doped SrTiO$_3$ ceramics prepared by sol-gel process and spark plasma sintering. *Solid State Sci.* **2010**, *12*, 1341–1346. [CrossRef]

164. Okinaka, N.; Zhang, L.; Akiyama, T. Thermoelectric properties of rare earth-doped SrTiO$_3$ using combination of combustion synthesis (CS) and spark plasma sintering (SPS). *ISIJ Int.* **2010**, *50*, 1300–1304. [CrossRef]

165. Kosyanov, D.Y.; Yavetskiy, R.P.; Tolmachev, A.V.; Vornovskikh, A.A.; Pogodaev, A.V.; Gridasova, E.A.; Shichalin, O.O.; Kaidalova, T.A.; Kuryavyi, V.G. Fabrication of highly-doped Nd^{3+}:YAG transparent ceramics by reactive SPS. *Ceram. Int.* **2018**, *44*, 23145–23149. [CrossRef]

166. Chaim, R.; Marder-Jaeckel, R.; Shen, J.Z. Transparent YAG ceramics by surface softening of nanoparticles in spark plasma sintering. *Mater. Sci. Eng. A* **2006**, *429*, 74–78. [CrossRef]

167. Podowitz, S.R.; Gaumé, R.; Feigelson, R.S. Effect of europium concentration on densification of transparent Eu:Y$_2$O$_3$ scintillator ceramics using hot pressing. *J. Am. Ceram. Soc.* **2010**, *93*, 82–88. [CrossRef]

168. Ma, H.J.; Jung, W.K.; Baek, C.; Kim, D.K. Influence of microstructure control on optical and mechanical properties of infrared transparent Y$_2$O$_3$-MgO nanocomposite. *J. Eur. Ceram. Soc.* **2017**, *37*, 4902–4911. [CrossRef]

169. Xu, M.; Chang, J.; Wang, J.; Wu, C.; Hu, F. Al$_2$O$_3$-YAG:Ce composite ceramics for high-brightness lighting. *Opt. Express* **2019**, *27*, 872–885. [CrossRef] [PubMed]

170. Liu, X.; Qian, X.; Hu, Z.; Chen, X.; Shi, Y.; Zou, J.; Li, J. Al_2O_3-Ce:GdYAG composite ceramic phosphors for high-power white light-emitting-diode applications. *J. Eur. Ceram. Soc.* **2019**, *39*, 2149–2154. [CrossRef]

171. Dehkordi, A.M. *An Experimental Investigation towards Improvement of Thermoelectric Properties of Strontium Titanate Ceramics*; ProQuest Dissertations and Theses; Clemson University: Clemson, SC, USA, 2014; Volume 76-02(E), ISBN 9781321220834.

172. Niwa, E.; Sato, K.; Yashiro, K.; Mizusaki, J. High-temperature gravimetric study on the kinetics of the formation of $SrTiO_3$ by solid state reaction of $SrCO_3$ and TiO_2. *ECS Trans.* **2009**, *16*, 205–210.

173. Ebrahimi, M.E.; Allahverdi, M.; Safari, A. Synthesis of high aspect ratio platelet $SrTiO_3$. *J. Am. Ceram. Soc.* **2005**, *88*, 2129–2132. [CrossRef]

174. Maca, K.; Pouchly, V.; Shen, Z. Two-step sintering and spark plasma sintering of Al_2O_3, ZrO_2 and $SrTiO_3$ ceramics. *Integr. Ferroelectr.* **2010**, *99*, 114–124. [CrossRef]

175. Sutharsini, U.; Thanihaichelvan, M.; Singh, R. Sintering of Functional Materials. In *Two-Step Sintering of Ceramics*; InTechOpen: London, UK, 2018; pp. 4–21.

176. Qin, M.; Gao, F.; Cizek, J.; Yang, S.; Fan, X.; Zhao, L.; Xu, J.; Dong, G.; Reece, M.; Yan, H. Point defect structure of La-doped $SrTiO_3$ ceramics with colossal permittivity. *Acta Mater.* **2019**, *164*, 76–89. [CrossRef]

177. Federicci, R.; Holé, S.; Popa, A.F.; Brohan, L.; Baptiste, B.; Mercone, S.; Leridon, B. $Rb_2Ti_2O_5$: Superionic conductor with colossal dielectric constant. *Phys. Rev. Mater.* **2017**, *1*, 032001. [CrossRef]